

Identification of filamentary structures in the environment of superclusters of galaxies in the Local Universe

Iris Santiago-Bautista^{1,2}, César A. Caretta², Héctor Bravo-Alfaro², Etienne Pointecouteau¹, and Heinz Andernach²

¹ IRAP, Université de Toulouse, CNRS/CNES/UPS, Toulouse, France
e-mail: isantiago@irap.omp.eu

² Departamento de Astronomía, DCNE-CGT, Universidad de Guanajuato, CP 36023, Guanajuato, Mexico
e-mail: isantiago@astro.ugto.mx

Draft, 2020

ABSTRACT

Context. The characterization of the internal structure of the superclusters of galaxies (walls, filaments and knots where the clusters are located) is paramount for understanding the formation of the Large Scale Structure and for outlining the environment where galaxies evolved in the last gigayears.

Aims. (i) To detect the compact regions of high relative density (clusters and rich groups of galaxies); (ii) to map the elongated structures of low relative density (filaments, bridges and tendrils of galaxies); (iii) to characterize the galaxy populations on filaments and study the environmental effects they are subject to.

Methods. We employed optical galaxies with spectroscopic redshifts from the SDSS-DR13 inside rectangular boxes encompassing the volumes of a sample of 46 superclusters of galaxies, up to $z = 0.15$. A virial approximation was applied to correct the positions of the galaxies in the redshift space for the “finger of God” projection effect. Our methodology implements different classical pattern recognition and machine learning techniques (Voronoi tessellation, hierarchical clustering, graph-network theory, minimum spanning trees, among others), pipelined in the Galaxy Systems-Finding algorithm and the Galaxy Filaments-Finding algorithm.

Results. We detected in total 2 705 galaxy systems (clusters and groups, of which 159 are new) and 144 galaxy filaments in the 46 superclusters of galaxies. The filaments we detected have a density contrast above 3, with a mean value around 10, a radius of about $2.5 h_{70}^{-1}$ Mpc and lengths between 9 and $130 h_{70}^{-1}$ Mpc. Correlations between the galaxy properties (mass, morphology and activity) and the environment in which they reside (systems, filaments and the dispersed component) suggest that galaxies closer to the skeleton of the filaments are more massive by up to 25% compared to those in the dispersed component; 70% of the galaxies in the filament region present early type morphologies and the fractions of active galaxies (both AGN and SF) seem to decrease as galaxies approach the filament.

Conclusions. Our results support the idea that galaxies in filaments are subject to environmental effects leading them to be more massive (probably due to larger rates of both merging and gas accretion), less active both in star formation and nuclear activity, and prone to the density-morphology relation. These results suggest that preprocessing in large scale filaments could have significant effects on galaxy evolution.

Key words. catalogs – galaxies: groups: clusters: superclusters – Large scale structure of the Universe– methods: data analysis

1. Introduction

The Large Scale Structure (LSS) of the Universe is composed of a network of groups and clusters of galaxies, elongated filaments, widely spread sheets, and voids (e.g. Peebles, 1980; Davis et al., 1982; Bond et al., 1996). Both, the Λ CDM cosmological model (e.g. Bond & Szalay, 1983; Doroshkevich & Khlopov, 1984) and recent numerical N-body simulations (e.g. Millennium, Springel et al., 2005; Bolshoi, Klypin et al., 2011; Illustris, Vogelsberger et al., 2014), reinforce that these structures are assembled under the effect of gravity, generated by the total matter content. Since the baryonic matter follows, to first order, the distribution of the dark matter, the galaxies and gas populate these substructures accordingly (e.g. Eisenstein et al., 2005). Moreover, there is increasing evidence that the galaxy properties (for instance mass, activity, morphology, luminosity, surface brightness, orientation, etc.) correlate with the LSS environment in which they are located (e.g. Smargon et al., 2012; Scoville et al., 2013; Poudel et al., 2016; Kuutma et al., 2017; Chen et al., 2017; Wang et al., 2018) or, more specifically, with the internal structure of the supercluster (e.g. Einasto et al., 2008;

Gallazzi et al., 2009; Gavazzi et al., 2010; Cybulski et al., 2014; Guglielmo et al., 2018). Furthermore, theoretical studies (e.g. Cen & Ostriker, 1999) suggest that from one half to two thirds of the baryonic matter in the Universe is hidden in the filamentary structures of the LSS. Therefore, the characterization of the LSS (e.g. topology, density, temperature, dynamical state, matter distribution and its evolution along time) is an important step to place constraints on the current cosmological models.

Galaxy clusters are well studied through their gas component since they are the densest regions of the LSS. However, the gas in filaments is most likely in a not so hot ($T \sim 10^5$ – 10^7 K, or 0.01–1 keV) and relative low-density gas phase called Warm Hot Intergalactic Medium (WHIM). There is already some evidence of such gas from X-ray emission observed within pairs of close clusters (e.g. Ursino et al., 2015; Alvarez et al., 2018). In addition, the WHIM between pairs of clusters has been observed through the Sunyaev-Zel’dovich effect (SZ, e.g. Planck Collaboration et al., 2013). Tanimura et al. (2018) carried out statistical analyses using Planck SZ observations in the regions of superclusters. Their results show evidence of inter-cluster gas

of temperature $T \sim 8 \times 10^6$ K. Also, [Eckert et al. \(2017\)](#) presented deep X-ray observations of the galaxy cluster Abell 2744, the analysis of which suggests a gas fraction of 5% to 15% for the filaments that surround the cluster and a plasma temperature of $1-2 \times 10^7$ K. Therefore, the characterization of these structures through observables like X-ray emission or Sunyaev-Zel'dovich effect is still challenging due to the low density and temperature of the WHIM.

An alternative is to analyze the galaxy distribution at large scales. Recently, with the availability of large sky area databases such as the Two Degree Field Redshift Survey (2dFRS, [Colless et al., 2001](#)), the 2MASS Redshift Survey (2MRS, [Huchra et al., 2012](#)) and the Sloan Digital Sky Survey (SDSS, [Albareti et al., 2017](#)), the development of accurate structure detection algorithms has become an even more important concern for astronomy. Visually, the galaxy distribution shows filamentary ridge-like structures that connect massive clusters and groups. However, the identification of these structures through a computational algorithm is not easy to achieve. A good algorithm should first produce an identification that resembles the human visual perception. It also should deliver quantitative results and be founded in a robust and well-defined numerical theory. All of this must be done in an acceptable amount of time with reasonable computational resources.

Currently, there are several filaments-finding algorithms that have been tested on the basis of N-body simulations. For example, [Aragón-Calvo et al. \(2007\)](#) present the “multi-scale morphology filter method” (*MMF*) that divides cosmic structure into nodes (clusters), filaments and walls by using a smoothing over a range of scales (from a Delaunay tessellation reconstruction, *DFTE*) and a morphological response filter. Another approach presented by [Aragón-Calvo et al. \(2010\)](#) makes use of a watershed segmentation techniques to trace the spines of the filaments. Also, [Cautun et al. \(2013\)](#) propose an algorithm that takes into account the density, tidal field, velocity divergence and velocity shear of the galaxies, called *NEXUS*. Other examples are the algorithms by [González & Padilla \(2010\)](#), which uses the binding energy for selecting the filament members; and the *DisPerSE* algorithm, by [Sousbie \(2011\)](#), based on the Morse theory – both utilize Delaunay-Voronoi tessellation based on density estimations.

On the other hand, several attempts were made to trace the distribution of the real cosmic web using the SDSS database. For example, the algorithm by [Bond et al. \(2010\)](#), called “smoothed Hessian major axis filament finder” (*SHMAFF*), was applied to the SDSS-DR6 after removing the “finger-of-God” (FoG) effect. [Platen et al. \(2011\)](#) compared three different reconstruction techniques, namely the *DFTE*, the “natural neighbor field estimator” (*NNFE*) and a *Kriging* interpolation, and searched for voids also in DR6. They found that *DFTE* works quantitatively better than the others while the *Kriging* and *NNFE* have a better performance in producing visually appealing reconstructions than *DFTE*. [Smith et al. \(2012\)](#) applied their “multi scale probability mapping” (*MSPM*), which combines probability and scale density information with a “Friends-of-Friends” (*FoF*) algorithm, over the SDSS-DR7 galaxies. Their method allowed them to recover structures from clusters to filaments of up to $\sim 10 h^{-1}$ Mpc. [Tempel et al. \(2014\)](#) applied a *Bisous* model on the SDSS-DR8 spectroscopic galaxies to trace the filament spines. Their method adjusts cylinders to the galaxy positions applying a stochastic metric. The “subspace constrained mean shift” (*SCMS*) approach, which uses a “kernel density estimator” (*KDE*), was applied by [Chen et al. \(2016\)](#) to DR7 and by [Chen et al. \(2015\)](#) to DR12. This method allows the identification of high density

regions by smoothing the galaxy distribution. They apply this technique over slices of 0.05 in redshift for the SDSS sky area. Moreover, [Alpaslan et al. \(2014\)](#) found, for the GAMA survey, that there are fine filaments embedded inside the SDSS voids. These structures, ‘tendrils’, have a lower density than the SDSS filaments and appear to be morphologically distinct, they are more isolated and span shorter distances. A comprehensive review and comparative analysis of these algorithms can be found in [Libeskind et al. \(2018\)](#).

Another approach to analyze the LSS structure is to study the superclusters of galaxies. These are traditionally defined as concentrations of galaxy clusters (e.g. [Abell, 1961](#); [Einasto et al., 2001](#); [Chow-Martinez et al., 2014](#)), building up the cosmic web from a network of connected high density nodes; or directly from the distribution of galaxies (e.g. [Luparello et al., 2011](#); [Costa-Duarte et al., 2011](#); [Liivamägi et al., 2012](#)). They can also be defined kinematically by mapping galaxy peculiar velocity flows, a technique still restricted to the very nearby Universe ([Tully et al., 2014](#); [Dupuy et al., 2019](#)). This last method is the closest to a purely gravitational potential based approach, and allows the identification of the “basins of attraction” that partition the Universe in cells or cocoons (e.g. [Dupuy et al., 2019](#); [Einasto et al., 2019](#)). For this work we adopted the supercluster second-order clustering definition for determining the superclusters of the sample. These systems are not virialized and the contents of the inter-cluster medium (dark matter halos, gas and galaxies) dynamically interact and organize by falling through the gravitational potential of the more massive structures, forming walls, filaments, groups and clusters. As shown in [Tanaka et al. \(2007\)](#), the possibility to find elongated chain-like structures increases in superclusters. Also, following the classification of superclusters by [Einasto et al. \(2014\)](#) in “filament-type” and “spider-type” ones, both have filaments, in a linear or radial configuration respectively. Following this approach, [Cybulski et al. \(2014\)](#), for instance, applied a combination of Voronoi tessellation and minimum spanning tree (*MST*) techniques over the Coma supercluster region in order to search for bridges between clusters of galaxies.

Motivated by the above context, we developed a methodology¹ for the identification of structures in the environment of superclusters using the galaxies embedded in them. We restrict our study to the SDSS-DR13 area, and use only galaxies with spectroscopic redshifts for our analysis. The approach we follow seeks to detect structures by using only the geometrical information of the galaxy distribution. By using different pattern recognition methods we identify high to moderate-density galaxy systems, and low-density filaments connecting them. This allows the identification of structures over a wide range of scales (1 – 100 Mpc), from groups to long filaments. Moreover, the identified structures are validated through comparisons with previously reported catalogs. We also carried out a qualitative validation through a kernel method which is one of the most used methodologies for the detection of overdensity regions. Our aim was to investigate whether previous filament candidates in the sample, identified from chains of Abell/ACO clusters, are bona-fide structures and to characterize their galaxy populations. Finally, we studied the relation between the galaxy properties and the supercluster environment in which they reside (e.g. systems, filaments and the dispersed component of the superclusters).

This paper is organized as follows: In Section 2 we present the data for the sample of superclusters under analysis and the

¹ https://gitlab.com/iris.santiagob89/LSS_structures

sample of galaxies from the SDSS survey. In Section 3 we describe in detail the implementation of mathematical tools and pattern recognition methods applied for the detection of high density regions (clusters and groups) and for the skeletonization of the low density filamentary structures. In Section 4 we describe the algorithm for detecting clusters and groups of galaxies inside superclusters' boxes, while in Section 5 we present the algorithm for finding the filaments and their skeletons. In Section 6 we describe the application of the algorithms to one of the superclusters, MSCC 310, as an example of their use. Section 7 is devoted to the validation and evaluation of the methodology and discussion of its results. In Sections 8 and 9 we present the results concerning the analyses of the galaxy properties as function of the supercluster environment. We also discuss these results and compare with previously reported results. Finally, in Section 10 we present the conclusions of this work. Through this paper we assume the Hubble constant $H_0 = 70 h_{70} \text{ km s}^{-1} \text{ Mpc}^{-1}$, the matter density $\Omega_m = 0.3$, and the dark energy density $\Omega_\Lambda = 0.7$.

2. The data

2.1. The superclusters and filament candidates

We are interested in unveiling and studying LSS filaments, which can be defined as chains of clusters connected by bridges of galaxies and probably by gas and dark matter. As mentioned previously, these elongated structures should most likely be found in superclusters since they probably just passed the quasi non-linear regime described by Zel'dovich's approximation (1970, see also the "sticking model" by Shandarin & Zel'dovich 1989). In the current evolutionary stage of LSS, superclusters are basically a network of sheets, filaments and knots (clusters and groups) of galaxies, gas and dark matter, just starting a global gravitational collapse process.

Thus, we selected a sample of superclusters of galaxies from the Main SuperCluster Catalogue (MSCC, Chow-Martínez et al., 2014), which are inside the SDSS region (in order to have a sample of galaxy data as homogeneous as possible). The original MSCC is an all-sky catalog that contains 601 superclusters, identified in a complete sample of rich Abell/ACO clusters, with updated redshifts from 0.02 to 0.15, by using a tunable *FoF* algorithm. From these superclusters, 166 are inside the SDSS Data Release 13 (DR13) region. For this work we selected those superclusters with 5 or more clusters having their box volume (see below) inside the SDSS-DR13 survey area. In addition, we used as reference the list of filament candidates for MSCC superclusters by Chow-Martínez et al. (in preparation), in order to select the superclusters with the most promising filaments. Roughly speaking, these filament candidates were identified as chains of at least three clusters, members of the superclusters, separated by less than $20 h_{70}^{-1} \text{ Mpc}$ from each other. The present work also intends to validate these filament candidates by searching for the bridges of galaxies that we expect to connect them. It is worth mentioning that some of the filament candidates may reveal to be only chance configurations, with no bridges of galaxies connecting the clusters of a chain. Also, some bridges may exist, but not necessarily along the straight lines connecting the clusters.

Our final sample consists of 46 superclusters of galaxies, which are listed in Table 1. The ID of the supercluster in MSCC is listed in column 1, with its proper name in column 2, when it exists. Column 3 presents sky coordinates, RA (α) and Dec (δ), of the supercluster mean position, while column 4 shows its mean redshift. Columns 5 and 6 list the richness (number of member clusters) and the number of filament candidates found

previously in each supercluster. The IDs of the Abell/ACO member clusters are listed in column 7.

For the Abell/ACO clusters and for the galaxies in the superclusters box volumes (see Section 2.3), we first transformed their radial-angular coordinates to rectangular coordinates as follows:

$$X = D_C \cos(\delta) \cos(\alpha), \quad (1)$$

$$Y = D_C \cos(\delta) \sin(\alpha), \quad (2)$$

$$Z = D_C \sin(\delta), \quad (3)$$

where D_C is the co-moving distance as obtained using the spectroscopic redshift and the cosmological parameters indicated above.

2.2. The SDSS galaxies

The main galaxy sample of SDSS-DR13 (Albareti et al., 2017) is a suitable database to search for filamentary structures on the LSS since: (i) it covers a large sky area (14,555 square degrees), containing various MSCC superclusters; (ii) it contains homogeneous photometric and spectroscopic data for galaxies with an astrometric precision of 0.1 arcsec rms and uncertainty in radial velocities of about 30 km s^{-1} (Bolton et al., 2012); (iii) it is roughly complete to the magnitude limit of the main galaxy sample ($r_{Pet} = 17.77$), which corresponds to an average $z \sim 0.1$, going (inhomogeneously) deeper for data releases after DR7 (Abazajian et al., 2009); (iv) at the limit of our sample, $z = 0.15$, the SDSS spectra are complete for galaxies brighter than $M_r \sim -21$.

SDSS-DR7 joins the SDSS-I/II spectra for one million galaxies and quasars. It has $\sim 6\%$ incompleteness due to fiber collisions (Strauss et al., 2002) and another $\sim 7\%$ incompleteness attributed to pipeline misclassification (Rines et al., 2007). These spectra are included in the final data release of the SDSS-III (Alam et al., 2015). The Baryon Oscillation Spectroscopic Survey (BOSS) is part of the SDSS-III observations and has obtained spectra for another 1.4 million galaxies. The BOSS observations are divided in two main samples, LOWZ ($z < 0.4$) and CMASS ($0.4 < z < 0.7$). The SDSS-DR13 (Albareti et al., 2017) includes spectra for more than 2.6 million galaxies and quasars.

Although photometric redshifts are available for SDSS galaxies, for this work we have selected those objects listed on the SpecObj sample with spectroscopic redshifts available (downloaded from the SkyServer web service) and denoting an extragalactic object (that is, galaxies and low- z quasars). The SpecObj table contains the best and unique spectra for the same location within 2 arcsec called "sciencePrimary" objects. We considered galaxies within a redshift range from 0.01 to 0.15 and selected spectra with quality flag "good" or "marginal". Since the kind of study presented here relies on the galaxy distance measurement, we restricted our analysis to galaxies with spectroscopic redshift due to its higher accuracy. However, galaxies with photometric redshift can be included to the sample in further analyses to test if their addition increase the filament signal of detection.

For the present work we also made use of value-added sub product catalogs such as the MPA-JHU catalog (Brinchmann et al., 2004; Kauffmann et al., 2003; Tremonti et al., 2004). They calculated different galaxy properties (stellar mass, metallicity, activity type classification, star forming rate, among others) using the spectra from the SDSS-DR8 galaxies (Aihara et al., 2011). As explained by Tremonti et al. (2004), the galaxy properties in the MPA-JHU catalog are calculated by processing the galaxy spectrum in a way that even the weaker emission lines

Table 1: Sample of MSCC superclusters used in the present work.

SCI ID (MSCC)	Name	RA, Dec [deg, deg]	\bar{z}	N_{Cl}	N_{fil}	Abell/ACO clusters
(1)	(2)	(3)	(4)	(5)	(6)	(7)
55		17.75, 15.44	0.0614	5	1	A0150 A0152A A0154B A0158B A0160B
72		25.17, 0.64	0.0802	5	1	A0181A A0208A A0237A A0267B A0279A
75		28.09, -5.15	0.0937	7	1	A0256A A0256B A0266 A0269 A0274A A0274B A0277
76		28.35, -2.61	0.1299	16	3	A0211 A0233e A0255 A0256C A0261B A0265 A0267C A0268B A0271 A0274C A0279B A0281 A0285 A0295D A0303C A0308e
175		125.29, 17.07	0.0942	6	1	A0635A A0650B A0651A A0657A A0658A A0659
184		130.10, 30.24	0.1056	6	1	A0671B A0690C A0694 A0695B A0699B A0705A
211		147.87, 64.88	0.1191	8	1	A0764 A0802 A0804B A0845 A0871e A0906e A0975 A1014A
219		153.99, 19.14	0.1155	5	1	A0938B A0942A A0952A A0991B A0994A
222		155.14, 49.21	0.1382	10	2	A0915B A0927A A0950A A0965A A0990 A1002A A1003C A1003D A1004 A1040C
223		155.24, 62.94	0.1399	5	1	A0917 A0947A A0962A A1025A A1025B
229		156.14, 33.03	0.1423	7	2	A0924 A0951 A0982 A1007B A1036 A1045 A1053B
236		156.76, 10.38	0.0328	6	1	A0938A A0957A A0999A A1016A A1020A A1142A
238		156.98, 39.55	0.1068	21	4	A0967A A0971A A0971B A0972A A0995A A0997A A0997B A0997C A1010B A1021B A1021C A1021D A1026B A1028A A1031A A1031B A1033 A1040A A1050A A1054A A1055
248		159.49, 44.26	0.1246	5	1	A1040B A1050B A1054B A1056 A1074A
264		165.29, 12.20	0.1161	8	1	A1105C A1116A A1129A A1141A A1147A A1157 A1201B A1209A
266		165.91, 11.85	0.1273	8	1	A1131 A1137B A1141B A1147B A1152 A1159 A1183A A1209B
272		167.83, 41.33	0.0760	6	1	A1173 A1174A A1187 A1190 A1193A A1203
277		169.41, 49.67	0.1103	7	1	A1154 A1202B A1218B A1222 A1225 A1227A A1231A
278	Leo	169.37, 28.46	0.0333	6	1	A1177B A1179B A1185A A1228A A1257A A1267A
283		170.79, 20.34	0.1379	12	3	A1177C A1188 A1230B A1232B A1242A A1243B A1247e A1251 A1268 A1272 A1274 A1278
295	Coma	173.63, 23.11	0.0223	5	1	A1100A A1177A A1179A A1367 A1656
310	UMa	175.91, 55.23	0.0639	21	3	A1212 A1270 A1291A A1291B A1291C A1318A A1318B A1324A A1324B A1349A A1349B A1377 A1383 A1396A A1396B A1400A A1400B A1400C A1436 A1452 A1457A
311		176.12, 9.93	0.0833	8	1	A1337A A1342A A1358A A1362B A1372A A1379 A1385A A1390
314		177.07, -2.01	0.0788	6	1	A1364A A1376A A1386A A1389A A1399A A1404A
317		177.42, -1.59	0.1278	13	2	A1373A A1373B A1376C A1386D A1386E A1386F A1389C A1389D A1392 A1399C A1407 A1411 A1419B
323		179.66, 27.26	0.1396	12	1	A1384A A1403A A1403B A1413B A1420C A1425B A1431B A1433C A1444C A1449B A1455C A1495
333		181.43, 29.34	0.0813	9	1	A1423A A1427 A1431A A1433A A1444B A1449A A1455B A1515A A1549A
335		182.42, 29.50	0.0732	6	1	A1444A A1455A A1478A A1480B A1486A A1519A
343		183.88, 14.31	0.0809	5	1	A1474 A1481A A1499A A1526C A1527A
360	Dra	190.94, 64.41	0.1055	11	1	A1518A A1539A A1544A A1559 A1566 A1579A A1621 A1640A A1646 A1674A A1718A
386		199.50, 38.33	0.0715	5	1	A1680A A1691 A1715A A1723B A1749B
407		208.55, 26.70	0.1364	6	1	A1797B A1817C A1817e A1818C A1819 A1824
414	Boo	211.31, 27.32	0.0709	24	3	A1775A A1775B A1781B A1795 A1797A A1800 A1817A A1818A A1831A A1831B A1832A A1863A A1869A A1869B A1873B A1873C A1874A A1886A A1898A A1903A A1908A A1909A A1912B A1921A
419		212.33, 7.17	0.1122	5	1	A1850 A1862 A1866A A1870 A1881
422		213.21, 28.95	0.1430	9	2	A1832B A1840B A1854 A1867A A1874B A1891B A1903C A1908B A1912E
430		216.72, 25.64	0.0982	6	1	A1909B A1910A A1912A A1912C A1926A A1927
440	BooA	223.17, 22.28	0.1170	9	1	A1939B A1972 A1976 A1980 A1986 A1988B A2001A A2006 A2021C
441		223.22, 28.40	0.1249	5	1	A1973A A1982D A1984 A1990A A2005B
454		228.28, 7.33	0.0456	6	1	A2020A A2028A A2033B A2040B A2055A A2063B
457		228.59, 6.98	0.0789	6	1	A2028B A2029 A2033C A2040C A2055B A2063C
460		229.70, 31.17	0.1142	9	1	A2025D A2034A A2049A A2056C A2059B A2062 A2067B A2069 A2083B
463	CrB	232.18, 30.42	0.0736	14	2	A2056A A2056B A2059A A2061A A2065 A2067A A2073A A2079A A2079B A2089 A2092A A2106A A2122A A2124
474	Her	241.56, 16.22	0.0363	5	2	A2147 A2151 A2152A A2153A A2159A
484		245.57, 42.39	0.1364	7	1	A2158B A2172 A2179 A2183 A2196 A2198D A2211A
579		351.82, 14.79	0.0427	5	1	A2572 A2589 A2593A A2593B A2657
586		354.20, 23.67	0.1274	5	1	A2611e A2619B A2627 A2647e A2650e

Notes. The superclusters have five or more Abell cluster members, with $z \leq 0.15$, and inside the SDSS-DR13 region. Superclusters with proper names are indicated in column 2.

are detectable. In order to analyze the morphological distribution of the galaxies in the different supercluster environments we employed the morphological classification provided by [Huertas-Company et al. \(2011\)](#). They calculate a probabilistic morphological classification, for the SDSS-DR7 spectroscopic galaxies, by applying deep learning techniques that make use of their photometry. They also compare their automated classification with a sample of the Galaxy Zoo ([Lintott et al., 2008, 2011](#)) visual classification. They show that their classification in early and late types are in good agreement with the visual classification.

2.3. The superclusters' boxes

For each supercluster in Table 1 we selected all the SDSS galaxies (according to the above criteria) located inside the corresponding box volume. These boxes were defined in rectangular coordinates, in a way that their walls were set at a distance of $20 h_{70}^{-1}$ Mpc beyond the center of the farthest clusters in each direction, for each supercluster. This extension was applied in order to guarantee that any connection of the supercluster with external structures could be detected. The box volumes of the superclusters vary from $(45 h_{70}^{-1} \text{ Mpc})^3$ to $(157 h_{70}^{-1} \text{ Mpc})^3$. Compared to

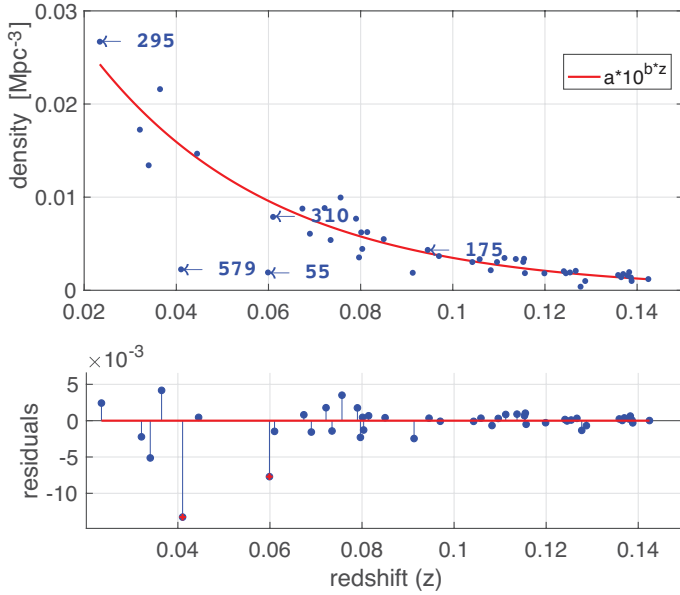


Fig. 1: Distribution of mean volume densities (see fourth column of Tab. 2), for the 46 superclusters in our sample, as function of redshift (blue points). The red line corresponds to the best fit of a power law function. Residuals of the fitting are shown in the bottom panel. MSCC 579 and MSCC 55 were excluded from the fitting.

the typical sizes of the observed and simulated basins of attraction in Dupuy et al. (2019) $[(50 - 100 h_{70}^{-1} \text{ Mpc})^3]$, the boxes we use here are a little bit larger, as expected, implying that we are sampling the LSS in a general way, not restricting the analysis to the densest parts of the superclusters. Our sampling of the superclusters may be compared to the one by Krause et al. (2013), that is, more embracing than the sampling done by, for example, Kopylova & Kopylov (2006) and Liivamägi et al. (2012).

In Table 2 we list the box volume (column 2), the number of galaxies inside this volume (column 3), its mean volume and surface (sky projected) number densities (columns 4 and 5), the baseline density (column 6), the number of galaxies with surface density above the baseline density (column 7), the segmentation parameter f and the number of *HC* groups (see Section 3.2 for details) (columns 8 and 9), the remaining FoG corrected groups of richness between 5 and 9 galaxies (column 10) and of richness higher or equal to 10 galaxies (column 11), the ranges of radius and velocity dispersion for this final list of groups (columns 12 and 13), for each supercluster.

In particular, the superclusters MSCC 236, MSCC 314 and MSCC 317 lie close to the limits of the SDSS region: although all their member clusters are inside, their boxes were reduced to a margin of $10 h_{70}^{-1} \text{ Mpc}$ in only one direction.

Figure 1 shows the diminution of mean volume density of the boxes with redshift, due to Malmquist bias. The fitted function will be used as the selection function for the SDSS galaxies considered in this work. It may be noted that the mean densities of the superclusters MSCC 55 and MSCC 579 lie far below the fit. This is also due to the positions of these superclusters close to the border of SDSS coverage: their samplings seem sparse and irregular. In fact, for MSCC 579 one can clearly see the shape of the cones of observation through the galaxy distribution. For this reason, the analysis of these superclusters and of the three cited above must be taken with caution.

It is worth noting that, since we have only the radial velocity component available (redshift), the transformation from radial-angular coordinates to rectangular coordinates is more complicated for the galaxies. Their peculiar velocity may bias their redshift-space coordinate, especially when they are members of clusters and groups of galaxies, being subject to the FoG effect. Thus, for the galaxy data used to detect the filaments, we first applied a correction, to be described below, which redefined their individual D_C in equations 1-3.

3. Mathematical tools

In what follows, we considered the N galaxies in each supercluster volume as a set of points $x_1, x_2, \dots, x_N \in X$, all part of a sample X .

3.1. Voronoi Tessellation (VT)

The Voronoi tessellation (Voronoi, 1908) of a sample X , $\text{Vor}(X)$, can be defined as the subdivision of a 2D plane or a 3D space into cells with the property that the seed point $x_i \in X$ is located in the cell v_i if and only if the Euclidean distance $D_E(x_i, v_i) < D_E(x_i, v_j)$ for each $v_j \in X$ with $j \neq i$. In other words, the VT divides the space into polygonal cells, centered on the seed points (in our case, galaxies), in a way that the cell walls are equidistant to all nearest seeds (e.g. Platen et al., 2011). Therefore, the density at each galaxy position x_i is determined as $d_i = 1/v_i$, with v_i being the volume (or area) of the cell enclosing the object x_i . Scoville et al. (2013) and Darvish et al. (2015), for instance, use VT to find the high density regions in sky slices while Cybulski et al. (2014) apply VT to identify the filamentary structures in the Coma cluster region.

3.2. Hierarchical Cluster Analysis (HC)

Hierarchical clustering is a machine learning method whose objective is to group objects with similar properties. It has been used in different areas of science such as artificial intelligence, biology, medicine and business. In general, it can be used to carry out pattern recognition analysis, allowing to regroup, segment and classify any kind of data. This method is equivalent to a reduction of the dimensionality of the data and reduces considerable the computing time. In astronomy, the most popular application of *HC* has been for the detection of substructures inside galaxy clusters, following the algorithm developed by Serna & Gerbal (1996). This algorithm considers the positions, redshifts and potential binding energy between pairs of galaxies to detect substructures (see also Guennou et al., 2014).

Since we are interested in finding galaxy structures on scales larger than the ones for substructures and for structures that may be less strongly gravitationally bounded, we chose to use an agglomerative hierarchical clustering analysis method that considers only the positions and redshifts or 3D estimated positions of galaxies. A detailed description of the *HC* algorithm can be found in Theodoridis & Koutroumbas (2009); Theodoridis et al. (2010) and Murtagh & Contreras (2011). For our analysis we chose Ward's minimum variance clusterization criteria, described in detail by Murtagh & Legendre (2014). In general, Ward's method works by merging the groups following the criterion:

$$\Delta D(c_1, c_2) = \frac{|c_1||c_2|}{|c_1| + |c_2|} \|c_1 - c_2\|^2. \quad (4)$$

where ΔD is a term that measures the distance between two groups c_1 and c_2 , respectively.

In our case, initially each point is considered as a group, sub-cluster or singleton, then each group can be agglomerated with a neighbor that has the minimum ΔD distance. The agglomeration continues until all points are grouped together.

The results of the *HC* clusterization can be represented by a dendrogram or hierarchical tree. A dendrogram represents, in a graphical form, the connections between elements and groups at different levels of agglomeration. The height of each connection line in the tree corresponds the distance between two elements or centroids connected. This representation also allows visualizing the principal branch structures where the singletons are the final leaves. The number of desired groups N_{cut} is, therefore, obtained by cutting the hierarchical tree at a certain level. The exact value of this level depends on the characteristics of the sample or, more properly, on the underlying physics that is used to define the groups.

Each created group can be represented by a 2D/3D Gaussian model, $P_j(x)$. This allows to classify the groups by their Gaussian properties, e.g. centroid (mean position, C_j), richness (number of members, N_j) and compactness (covariance, σ_j).

3.3. Graphs

Graph theory-based algorithms have shown to be a suitable tool to analyze complex networks. Some of the most common subjects where these algorithms are applied successfully are social networks, computer vision, statistics, business and transportation networks.

A graph is a representation of the connections in a network. It is composed of “nodes” and “edges”, where each node represents an object, and the edges represents the connections between each two nodes. Also, the edges can have weights that represent the strength of the connection. An undirected graph has edges that do not have direction. We can define an undirected graph as $G = (U, E, W)$, with n nodes (or vertices) $u_i \in U$, m edges $e_{kl} \in E$ and a weight set W with a w_{kl} for each edge e_{kl} . The information of a graph can be represented by a square adjacency matrix. The values of the matrix entries indicate the weight of the connection between nodes. Hence, the adjacency matrix A of the graph G is defined as:

$$[A]_{kl} = \begin{cases} 1 & \text{if } (u_k, u_l) \in E \\ 0 & \text{otherwise} \end{cases}$$

where u_k and u_l are nodes in G . One can refer to [Ueda & Itoh \(1997\)](#) for a discussion about the use of graph theory approach for quantifying the LSS of the Universe.

3.4. Minimum Spanning Tree (MST)

A spanning tree connects all nodes in a graph in a way that does not produce cycles. A graph can contain several unconnected spanning trees. Since the edges in a graph can have weights, the minimum spanning tree algorithm ([Graham & Hell, 1985](#)) searches for a spanning tree that minimizes the total weight. This algorithm traces a tree-like continuous path for a group of edges and nodes in an optimal way. In particular, the Kruskal minimum spanning tree algorithm analyzes the edges in sequence, sorting them by weight. At the beginning, the shortest edge is analyzed and this would be the first tree branch. Then, the nodes are added to the tree under three conditions: (i) only one node is added to

the tree; (ii) a node is added based in the number of connected edges; (iii) their edges cannot be connected to another existing node in the tree. The process continues with the following edges in the graph until all connected edges are analyzed. Finally, the tree is extracted from the graph and the process begins again with the remaining nodes until all are tested. As its name remarks, the result is a forest of optimized independent trees.

3.5. Dijkstra's shortest path

Dijkstra's algorithm ([Dijkstra, 1959](#)) is a classical method for searching the shortest path between two nodes in a graph. We define a path of length e_{kl} between two nodes u_k and u_l as a sequence of connected nodes u_1, u_2, \dots, u_n if $k \neq l \forall k, l \in 1, \dots, n$. In general Dijkstra's algorithm works as follows.

First, an origin is selected by taking the node at the beginning of the path, u_0 . Then, a distance value is assigned to all nodes: set as zero for the origin, $s(u_0)$, and as infinity for all the other nodes, $s(u_i) = \text{inf}$. Next, all nodes are marked as unvisited and u_0 is marked as current a . The algorithm then calculates the distance from the current node a to all the unvisited nodes connected by the edges e_i as $s_{new} = s(e_{ai}) + w_{ai}$; here $s(e_{ai})$ is the distance from a to the node u_i and w_{ai} is the weight of the edge e_i . If $s(e_{ai}) + w_{ai} < s(e_i)$, then the distance is updated and the connected node label is updated as the current a . After visiting all neighbors of the current node, they are marked as visited. A visited node will not be checked again; then the recorded distance $s(e_{ai})$ is final and minimal. Finally, if all nodes have been visited, the algorithm stops. Otherwise, the algorithm sets the unvisited nodes with the smallest distance (from the initial node u_0 , considering all nodes in the graph) as the next “current node” and continues from the second step. A detailed description of the algorithm can be consulted in [Santanu \(2014\)](#).

3.6. Kernel Density Estimator (KDE)

As mentioned before, *VT* is used to measure the local density at each point position. However, in some cases, it fails on the identification of large overdensity regions, as mentioned by [Cybulski et al. \(2014\)](#). An alternative for the *VT* method is to apply kernel density estimators. In general, *KDE* methods work by adjusting a kernel function over each observation in the sample. However, the choice of the optimal kernel model and its intrinsic parameters is still under investigation in the pattern recognition community. Also, there are several attempts to apply adaptive Gaussian model kernels, in other words, to change the size of Gaussian model as a function of different parameters, for instance the distance to the nearest neighbor ([Chen et al., 2016](#)) or a weighting function ([Darvish et al., 2015](#)).

For this work we used the results from the *VT* method (see Section 3.1) as the input parameters for the *KDE*. We start by fitting an ellipsoid inside each *VT* cell. Thus, instead of choosing a fixed bandwidth for the kernel, we employ the eigenvalues and eigenvectors of the ellipsoids to calculate a Gaussian kernel ϕ_{Σ} centered at μ with covariance matrix Σ for each observation. Therefore, each n -dimensional kernel is represented as:

$$\phi_{\Sigma}(\mathbf{x} - \mu) = (2\pi)^{d/2} |\Sigma|^{-1/2} e^{-1/2(\mathbf{x}-\mu)^T \Sigma^{-1}(\mathbf{x}-\mu)}. \quad (5)$$

Then the *KDE* can be estimated as:

$$\hat{p}_{\text{KDE}}(\mathbf{x}) = \sum_{i=1}^N \alpha_i \phi_{\Sigma_i}(\mathbf{x} - \mathbf{x}_i), \quad (6)$$

where α_i is a weight factor calculated from the VT cell volume (v_i) as $1/v_i$.

The identification of the overdensity regions is done through the projection of KDE kernels in 2D planes superposing a regular rectangular grid to the data. Thus, the density estimation is obtained at each grid intersection by calculating the average density of all kernels that overlap at that point. Then, observations closer to an evaluating point will contribute more to the density estimation than points farther away from it. Consequently, the density will be higher in areas with many observations than in areas with few observations.

3.7. Transversal profiles

The distribution of galaxy properties in filaments is analyzed by constructing transversal profiles. These profiles are calculated by setting up a series of concentric cylinders with axes orientated along the filament skeletons. Then, a bin is considered to be the volume within two concentric cylinders of radius R_{cy} and $R_{cy} + \Delta R_{cy}$. The occurrence of a galaxy proxy in each bin is determined with respect to the galaxy distance from the filament skeleton D_{ske} . The total count of galaxies per bin is weighted by the bin volume, in a similar way as making a normalized histogram. In order to compare samples of different sizes, a normalization is applied by dividing the number of events in a bin by the total number of galaxies in the sample.

4. Galaxy Systems-Finding algorithm (GSyF)

4.1. Detection of high density regions

We first searched for the high relative density regions, clusters and groups of galaxies (which we will refer generically as galaxy systems), inside the studied superclusters, since these systems are the natural nodes for filaments. This was also necessary for correcting the FoG effect and having the data prepared for the application of the filaments-finding algorithm (see next Section). Furthermore, the detection of galaxy systems allows the identification of new ones possibly not known before (especially poorer galaxy groups), and the improvement of the membership estimation of the superclusters themselves.

A description of the algorithm, including the strategy we used for optimizing its parameters using simulated mock volumes, is presented in [Santiago-Bautista et al. \(2019\)](#). Here we review the main steps of this algorithm. First we calculate the local surface density at the position of each galaxy in the projected area of the supercluster by applying the VT method (section 3.1). The VT individual area of the galaxy can be directly converted to a surface density estimation ($d_i = 1/\alpha_i$), in this case in units of deg^{-2} . It is worth to note that the boxes we have considered for the superclusters in our sample comprehend slices in redshift-space in a range between $0.02 \leq \Delta z \leq 0.07$.

In order to identify the galaxy systems, we start by applying the HC method (section 3.2), but only to the N_{gal} galaxies with densities above a baseline density, d_{bas} , which should be analogue to a background density. In a certain sense, this separates supercluster galaxies from void galaxies (that is, under-dense regions). This baseline is calculated from the mean density by randomizing the galaxies in each sky projected area. Since the distribution of points in the space is not isotropic, it is not possible to set directly a background density from the projected positions of the galaxies. Therefore, it is necessary to simulate an isotropic distribution of the points, in order to set the baseline value (see, e.g. [Cybulski et al., 2014](#)). A set of 1 000 randomization of the

points positions is generated, each with the same sample number over the same area. Then, the mean surface density is calculated by:

$$d_{bas} = \frac{1}{m} \sum_{j=1}^m \frac{1}{n} \sum_{i=1}^n d'_{i,j}, \quad (7)$$

where $d'_{i,j} = 1/\alpha'_{i,j}$ corresponds to the inverse of the area of the point x'_i for the randomization j .

Since the distribution of galaxies is not homogeneous among the different boxes, we calculate independent baseline values for each supercluster, see Table 2. A density contrast (δ_i) is then calculated as:

$$\delta_i = \frac{d_i - d_{bas}}{d_{bas}}. \quad (8)$$

That is, the N_{gal} galaxies to which we apply the HC are the ones with a density contrast, $\delta_i > 0$ (see [Santiago-Bautista et al., 2019](#), for an evaluation of the negligible effect of slightly changing the density threshold).

Then, we apply HC to the set of parameters (RA, Dec, $1000z$) for these galaxies (the factor of 1000 is the weight for z values to be comparable to the sky coordinates values). The number of groups taken from the analysis is defined as a cut of the HC tree, fixed to $N_{cut} = N_{gal}/f$, with a segmentation parameter f , which is the expected mean number of elements per group. Currently, the selection of the optimal number of groups in clusterization methods is still a topic under investigation in the pattern recognition community, which includes the HC algorithm. A specific value of f was calculated for each supercluster ($3 \leq f \leq 36$) according to the optimization process described in [Santiago-Bautista et al. \(2019\)](#). This strategy was adopted because a physically motivated value for f would depend on many parameters, like the density of galaxies in each box, the sampling of these galaxies with respect to the real distribution, the redshift, among others which are difficult to estimate for our data.

Finally, we select only those systems with a number of galaxies, N_j , larger than two. These pre-identified systems are, then, subject to the next step of refinement: the iterative estimation of the dynamical parameters virial mass and radius.

4.2. FoG correction

After identifying the galaxy systems we proceed to refine the galaxy membership and correct the galaxy positions for the FoG effect by using a virial approximation. We apply a simplified version of the algorithm presented by [Biviano et al. \(2006\)](#) for the estimation of the virial mass and radius. We do not apply the surface pressure term correction based on the concentration parameter. Avoiding such a correction can lead to an overestimation of the virial radius, however, for this geometric analysis, only a virial approximation is enough.

The virial parameters calculation algorithm works as follows: First we take the projected center and mean velocity of the system from the results of HC (C_j). The projected center is then set at the position of the brightest r -band magnitude member galaxy (BMG) within $1 \sigma_j$ from the HC center, while the HC mean velocity is used directly. Those galaxies expected to belong to the system are selected among all galaxies in the sample (those with spectroscopic redshift in SDSS-DR13) that are projected inside a cylinder of radius R_a , hereafter, aperture. [Biviano et al. \(2006\)](#) show that the dynamical analyses are similar for different aperture sizes. We chose an aperture of $R_a = 1 h_{70}^{-1} \text{ Mpc}$.

Then, for the line-of-sight direction, we select galaxies with a difference in velocity up to $S_a = \pm 3000 \text{ km s}^{-1}$ with respect to the mean cluster velocity. This would correspond to three times the velocity dispersion of a rich cluster. A robust estimation of mean velocity, v_{LOS} , and velocity dispersion, σ_v , for the galaxies inside the cylinder is obtained by using Tukey’s biweight method (Beers et al., 1990). An approximation of the mass M_a in the aperture is computed as:

$$M_a = \frac{3\pi}{2G} \sigma_v^2 R_h, \quad (9)$$

where G is the gravitational constant, the $3\pi/2$ is the deprojection factor and R_h is the projected harmonic radius.

We calculate the virial radius, $R_{vir}^3 = (3/4\pi)(M_{vir}/\rho_{vir})$, by assuming a spherical model for nonlinear collapse, that is, by taking the virialization density as $\rho_{vir} = 18\pi^2[3H^2(z)]/[8\pi G]$, and M_a as an estimation for M_{vir} , we have:

$$R_{vir}^3 = \frac{\sigma_v^2 R_h}{6\pi H^2(z)} \quad (10)$$

Then, the aperture R_a is updated to the calculated R_{vir} value, the mean velocity to v_{LOS} , and S_a to σ_v , defining a new cylinder. This process is repeated iteratively until the radius R_{vir} converges. M_{vir} is finally calculated at the end of the iteration process.

The correction for the FoG effect is carried out by adjusting the position of the N_{mem} galaxies inside the final cylinder. This is done by scaling their comoving distances along the cylinder to the calculated virial radius.

A schematic representation of the GSyF algorithm, including the FoG correction, can be found on the left side of Figure 2.

5. Galaxy Filaments skeleton-Finding algorithm (GFIF)

5.1. Detection of low density regions

Since we are interested in the detection and analysis of elongated and low relative density contrast structures, we apply again a combined *VT+HC* method to the data, but now in the rectangular 3D space, with the positions of the galaxies corrected for the FoG effect. Thus, the *VT* densities are now volume densities, in units of Mpc^{-3} . At the beginning of this analysis the *HC* method is applied to all galaxies in the volume without density restrictions, that is, no baseline is applied. Density restrictions are considered later as criteria for the construction of filaments. Another difference between this application of *VT+HC* and the one used for the GSyF methodology is a relaxed cut in the hierarchical tree. Since we are interested in detecting more elongated representative structures, we tested values for the segmentation parameter f between 10 and 40. The direct effect of relaxing the cut is to allow the detection of groups at lower densities.

Here we need to make some practical definitions in order to describe our strategy.

- The nodes to which we will apply the method correspond, in the context we are working, to the *HC* group centroids.
- An edge is defined as any connection between two nodes.
- The real “links” between the systems are defined as the most promising edges, filtered according to their proximity and density contrast.
- Spanning trees are extracted as described in section 3.4, by cutting the graph in no-cycled optimal trees. Some nodes inside a spanning tree may have been detected as galaxy systems by the GSyF algorithm.

- A “bridge” is defined as a sequence of links and nodes between two systems.
- A “filament” is identified if a spanning tree bridges three or more systems connected by bridges.
- If the spanning tree contains none or only one system, it is called “tendrils”.
- The “skeleton” is the medial line of a filament. The method for finding it, which intends to reduce the dimensionality of the objects (in our case, galaxy filaments), is known as skeletonization.

Figure 3 shows schematically these definitions.

5.2. Chaining the filaments

Once we have applied *HC* we measure the Euclidean distance D_E of each group’ centroid (node) against all its group neighbors. These connections (edges) can be represented by an undirected graph as described in section 3.3. The weights W of the edges are set by the Bhattacharyya coefficient, BC , defined as:

$$BC(P_1, P_2) = \sum_{x \in X} \sqrt{P_1(x)P_2(x)}. \quad (11)$$

The Bhattacharyya coefficient quantifies the amount of overlapping between two distributions $P_1(x)$ and $P_2(x)$. Thus, the orientation of the two groups weights the connection between them.

In the next step, we filter the edges by two criteria: First we select the edges corresponding to a D_E smaller than a threshold, D_{max} (hereafter, linking length). Secondly, we consider an edge as a real link of galaxies based on the following: i) we define a cylinder along the edge with radius of $1 h_{70}^{-1} \text{ Mpc}$; ii) we measure the linear density of galaxies along the cylinder; iii) if the mean linear density of the cylinder is above $d = N/V$ (Table 2) we take the cylinder as a link of galaxies connecting the two nodes.

Each ensemble of connected links is a tree in the forest graph. We then apply Kruskal’s *MST* technique (section 3.4) on the forest graph to identify independent trees and their dominant branches.

To proceed we need to match the list of detected spanning trees with the list of detected GSyF systems. However, due to the effect of losing sampled galaxies with increasing redshift (see Figure 1), the richness of the detected systems depends on the redshift. In other words, to have a comparable richness for two similar system, for instance one at $z = 0.03$ and the other at $z = 0.13$, we have to apply a correcting factor to the richness of the second one. To overcome this limitation, we apply the following lower limit for the richness of the systems at the supercluster redshift: $\log_{10} N_{min} = a \log_{10} z + b$, with $a = -1.0$ and $b = -0.2$. This leads to a lower richness limit of $N_{min} = 30$ to 5 galaxies per system, from the nearest and farthest supercluster in our sample respectively.

Having now the systems and the bridges between them (instead of the nodes and edges in the previous step) we can identify the filaments. As stated above, and following the definition by Chow-Martínez et al. (in preparation), we search for the filaments which have at least 3 galaxy systems connected by bridges.

Although isolated bridges (that is, connecting only one pair of systems) and tendrils (connections between nodes with no system embedded) are important and are also a sub-product of the algorithm, we will focus our discussion hereafter only on the filaments. The connecting edges of these filaments are then refined using Dijkstra’s algorithm (section 3.5). This refinement

Table 2: Properties of the supercluster boxes and of the galaxy systems detected inside them by GSyF algorithm.

SCI ID (MSCC) (1)	V [$10^3 h_{70}^{-3} \text{ Mpc}^3$] (2)	N (DR13) (3)	$d = N/V$ [$h_{70}^3 \text{ Mpc}^{-3}$] (4)	$d_{surf} = N/A$ [deg^{-2}] (5)	d_{bas} [deg^{-2}] (6)	N_{gal} $d_i > d_{bas}$ (7)	f (8)	N_{HC} $N_j \geq 3$ (9)	$N_{mem} < 10$ (10)	$N_{mem} \geq 10$ (11)	R_{vir} [$h_{70}^{-1} \text{ Mpc}$] (12)	σ_v [km s^{-1}] (13)
55	424.3	812	0.0019	77.6	8.3	468	27	57	11	5	1.1 - 2.4	245 - 806
72	549.7	1941	0.0035	232.0	22.1	1341	18	228	30	22	0.9 - 2.4	184 - 689
75	854.6	1607	0.0019	95.8	22.6	877	15	69	9	7	1.5 - 3.4	335 - 1144
76	2628.3	2617	0.0010	110.1	26.6	1536	27	204	14	11	1.3 - 3.6	214 - 1051
175	577.4	2504	0.0043	116.3	25.8	1315	6	172	22	10	1.2 - 2.7	220 - 735
184	692.9	2101	0.0030	70.5	20.7	1003	3	137	10	9	1.4 - 2.7	278 - 739
211	814.7	1484	0.0018	28.6	11.5	654	6	53	2	3	1.9 - 2.1	406 - 496
219	628.4	1913	0.0030	118.2	19.5	1273	6	175	13	10	1.4 - 3.7	292 - 1151
222	955.9	1865	0.0020	97.3	20.3	885	3	123	10	8	1.3 - 4.1	245 - 1207
223	777.0	776	0.0010	302.7	13.8	247	3	45	1	3	2.1 - 2.1	475 - 475
229	1352.4	1855	0.0014	45.2	22.3	745	3	106	6	2	2.2 - 2.2	498 - 498
236	643.6	8636	0.0134	52.9	10.3	4733	3	309	93	73	0.5 - 1.8	105 - 703
238	3861.8	8328	0.0022	74.4	20.3	4860	6	832	38	74	0.7 - 4.0	112 - 1293
248	690.1	1263	0.0018	72.4	17.4	564	3	75	5	2	1.7 - 2.8	366 - 730
264	923.7	1704	0.0018	59.6	24.5	626	3	105	11	12	1.3 - 3.5	245 - 1026
266	458.5	958	0.0021	49.5	28.8	318	3	55	6	3	1.6 - 3.1	320 - 823
272	138.4	1379	0.0100	135.3	28.0	654	3	87	10	5	1.1 - 2.4	219 - 699
277	905.3	2748	0.0030	76.0	20.2	1329	6	179	17	9	1.4 - 2.5	278 - 675
278	459.3	7920	0.0172	52.3	10.3	4116	6	222	80	35	0.5 - 1.9	112 - 711
283	1478.8	2320	0.0016	70.3	20.2	1379	12	239	10	17	1.5 - 3.4	295 - 907
295	535.5	14308	0.0267	48.5	7.2	7422	6	272	114	46	0.4 - 2.0	74 - 909
310	1558.8	12286	0.0079	76.9	15.7	7529	6	1015	116	139	0.8 - 3.0	140 - 1182
311	958.8	5270	0.0055	91.8	22.4	3050	6	416	48	40	0.8 - 2.4	131 - 704
314	91.9	558	0.0061	135.2	27.0	289	3	49	10	4	1.2 - 2.3	254 - 659
317	438.6	840	0.0019	104.2	38.2	433	6	76	10	5	1.8 - 3.3	366 - 929
323	1909.6	3330	0.0017	77.3	21.7	1764	6	304	17	21	1.5 - 3.7	295 - 1069
333	445.5	1968	0.0044	65.1	22.6	793	3	135	14	27	1.1 - 2.9	221 - 949
335	574.5	3099	0.0054	62.2	21.4	1285	3	211	29	38	0.8 - 3.0	144 - 973
343	427.9	2679	0.0063	105.8	19.2	1526	6	196	23	25	0.8 - 2.4	131 - 675
360	657.7	2199	0.0033	80.1	15.3	934	12	160	15	16	1.3 - 2.5	253 - 653
386	535.9	3256	0.0061	54.9	17.2	1600	9	257	33	40	1.0 - 2.7	211 - 852
407	800.0	1126	0.0014	48.9	22.8	481	12	79	5	5	1.5 - 4.0	280 - 1184
414	1245.9	10902	0.0088	93.0	23.1	6366	6	1066	144	161	0.8 - 3.2	140 - 1191
419	497.6	1723	0.0035	91.7	19.7	1103	6	196	25	20	1.2 - 3.3	211 - 976
422	884.6	1065	0.0012	41.9	24.2	382	3	62	2	6	2.1 - 2.3	474 - 526
430	437.0	1603	0.0037	88.6	22.9	871	3	121	20	9	1.3 - 2.4	281 - 647
440	1017.1	3442	0.0034	99.4	72.9	917	6	143	24	14	1.5 - 3.3	309 - 935
441	516.1	1058	0.0021	60.8	20.9	425	6	59	2	3	3.0 - 3.0	796 - 796
454	389.0	5704	0.0147	99.7	18.9	3231	6	524	84	106	0.7 - 1.9	142 - 610
457	529.6	4072	0.0077	129.0	22.7	2605	6	443	58	44	1.0 - 3.1	187 - 1038
460	1041.1	3499	0.0034	108.4	27.3	1925	3	335	35	23	1.3 - 3.6	238 - 1073
463	959.2	8466	0.0088	121.6	22.4	5278	3	898	113	113	0.6 - 3.1	103 - 1077
474	343.8	7424	0.0216	109.2	15.3	4506	9	166	64	26	0.6 - 2.6	122 - 1115
484	805.0	1319	0.0016	43.1	19.2	571	6	86	5	4	2.3 - 3.0	536 - 793
579	658.9	1477	0.0022	142.9	1.2	1234	3	149	19	23	0.6 - 1.9	128 - 659
586	962.1	373	0.0004	18.3	13.6	72	3	8	0	0	-99.0 - -99.0	-99 - -99

Notes. The value -99 is set when GSyF does not detect systems.

allows the identification of the filament skeleton, i.e. the principal branch connection. According to the pattern recognition literature, a skeleton represents the principal features of an object such as topology, geometry, orientation and scale. Figure 4 shows schematically the steps of the GFIF algorithm.

The results of the filaments-finding algorithm depend on several parameters, in particular the number of HC groups, N_{cut} (or, equivalently, f), and the linking length D_{max} . Therefore, it is necessary to carry out a search for the optimal combination of these parameters. In addition, in order to find the longest filaments possible inside the supercluster volume, we search for the linking length that maximizes the number of filaments in the box, that is just before they begin to percolate. The optimization for these parameters is described in detail in Santiago-Bautista et al. (2019). We found that the optimized parameter f decreases with z from about 20 to 10 galaxies in the range covered by our sample, that is, depending on the sampling, a smaller density is found

with increasing z . The D_{max} , in turn, increases with z , in a way to compensate the decrease in f .

A schematic representation of the GFIF algorithm can be found on the right side of Figure 2.

6. Detection algorithms in action

In order to illustrate the detection algorithms presented above, we now describe their application to one of the superclusters in our sample, MSCC 310, the *Ursa-Majoris* Supercluster (see Tables 1 and 2). This supercluster contains 21 Abell clusters, with redshifts in the range from 0.05 to 0.08, and it is one of the largest in volume in our sample: it occupies an area in the sky of about 1700 deg^2 , equivalent to a volume of $(116 h_{70}^{-1} \text{ Mpc})^3$ (including the $20 h_{70}^{-1} \text{ Mpc}$ added to the box limits from the farthest clusters).

The volume contains $N = 12286$ SDSS galaxies with spectroscopic redshift. This corresponds, to a mean surface density

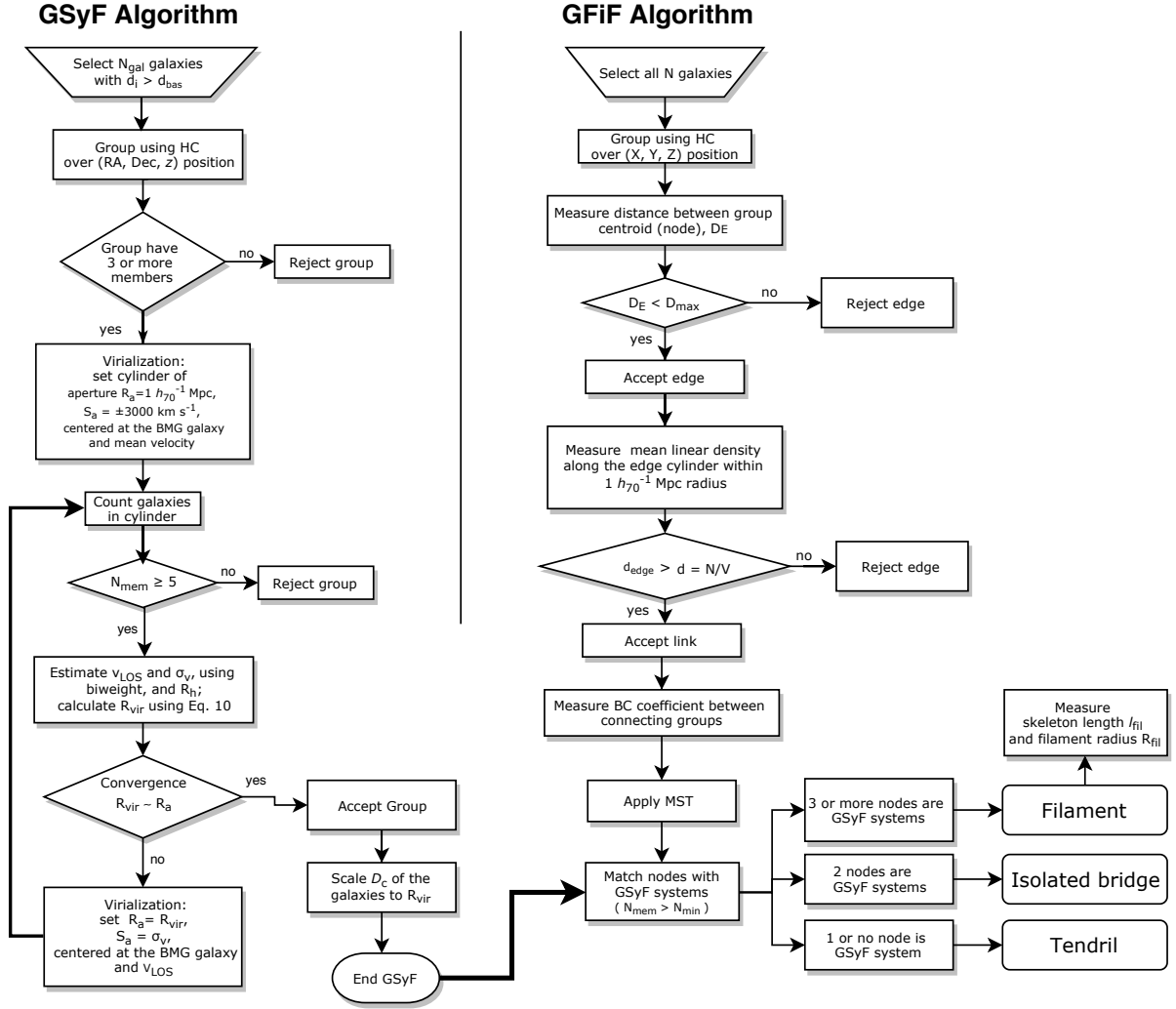


Fig. 2: Flow chart of the GSyF (left side) and GFIF (right side) algorithms.

of $76.9 \text{ gal.deg}^{-2}$ or $0.008 \text{ gal.}h_{70}^3 \text{ Mpc}^{-3}$, see Table 2. The list of parameter values used is shown in Table 5.

6.1. Application of GSyF to MSCC 310

First we applied the VT algorithm to the projected distribution of MSCC 310 galaxies and calculated their d_i . Then we made 1 000 simulations to estimate d_{bas} (15.7 deg^{-2} , for this case). We applied the HC algorithm to the $N_{gal} = 7\,529$ galaxies with $\delta_i > 0$. After calculating the best f parameter from the 30 mock simulations ($f = 6$, in this case), we have taken the $N_{cut} = 1\,140$ groups generated from the HC application. As expected, these groups have, on average, ~ 6 members. Of these, we retained 1 015 with $N_j \geq 3$.

The iterative virial refinement was initialized by assigning the center of each HC group at the brightest r-band galaxy member close to its geometrical centroid (see Table 3). For MSCC 310 groups, the mean difference between the geometrical center and brightest groups' galaxy projected position was found to be about $350 h_{70}^{-1} \text{ kpc}$. On average, the virial refinement needed six iterations to produce convergence to the virial radius. This refinement resulted in 122 systems with $N_{mem} \geq 10$ for the MSCC 310 volume. The refinement also detected 113 smaller systems with $5 \leq N_{mem} < 10$.

In Table 3 we list the properties of the first 25 richest systems for the MSCC 310 supercluster. Column 1 assigns a sequential number to the systems, while column 2 presents their richness. The coordinates of the brightest member of the system are indicated in columns 3, 4 and 5, while columns 6, 7 and 8 show the coordinates of the final position of the centroid. The other calculated properties of the systems – velocity dispersion, harmonic and virial radius – are presented in columns 9, 10 and 11 respectively. Column 12 denotes the cross-reference with Abell clusters. The range of virial radii of the GSyF systems with $N_{mem} \geq 10$ in MSCC 310 was $0.7 - 2.5 h_{70}^{-1} \text{ Mpc}$. For groups with $5 \leq N_{mem} < 10$ the range of virial radius lies within $0.4 - 0.9 h_{70}^{-1} \text{ Mpc}$. After the refinement, the projected central position of the systems changed, on average by $170 h_{70}^{-1} \text{ kpc}$, while the redshift was refined for some cases up to $\Delta z \sim 0.001$ or $\Delta\sigma_v \sim 300 \text{ km s}^{-1}$.

As an example, the richest system in MSCC 310 is the cluster A1291 A. Its HC initial centroid position (set as the position of the brightest galaxy in the HC group: $\alpha = 172.73$, $\delta = 56.49$ and $z = 0.0611$) changed by $13 h_{70}^{-1} \text{ Mpc}$ after 17 iterations of the virial refinement (the final centroid position corresponds to $\alpha = 173.01$, $\delta = 56.09$, $z = 0.0535$). This position is at $240 h_{70}^{-1} \text{ kpc}$ from the system's brightest galaxy detected for A1291 A which

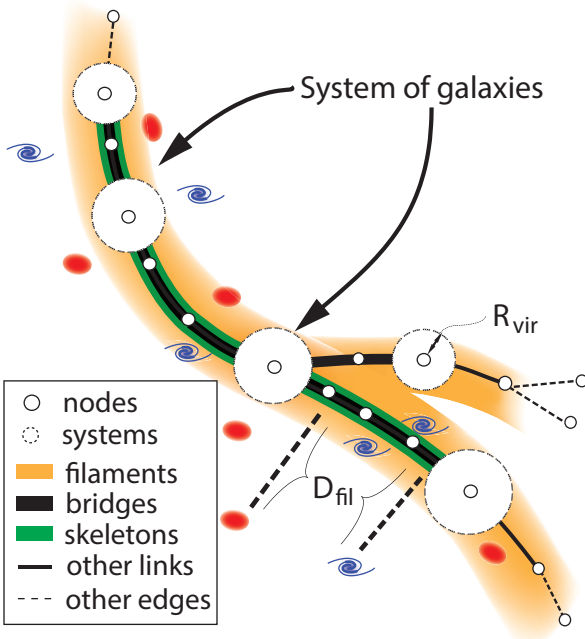


Fig. 3: Representation of a filament. Graph nodes are represented by white circles and edges by dark lines. The five systems connected are represented by a dotted circle of radius R_{vir} . A bridge connecting two systems is represented as a bold black line. The distance from galaxies to the filament (bold dashed line) is measured perpendicularly respect to the edges.

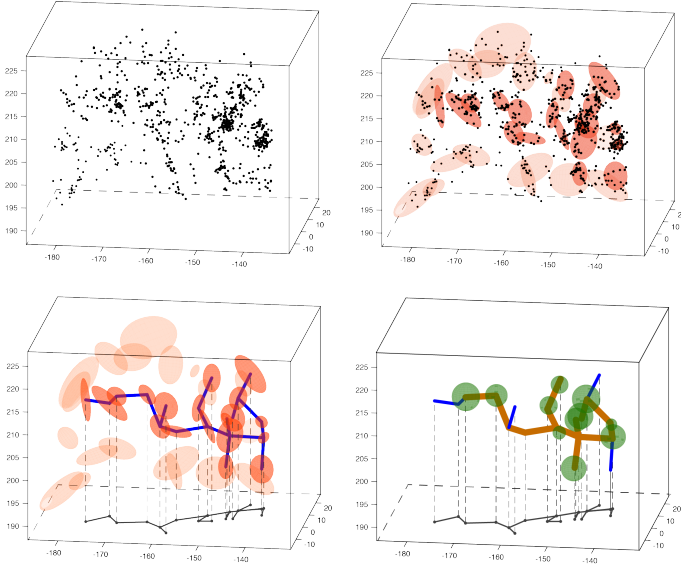


Fig. 4: Illustration of the steps of the GFIF algorithm. In the first box (top-left) one can see the distribution of galaxies. In the second one (top-right) the HC groups are marked, with denser red colors representing the richer HC groups. The filtered edges (links) among the groups of the spanning tree are displayed in the third box (bottom-left). The last box (bottom-right) presents the systems (green circles), bridges (brown lines) and other links (blue lines) found among the groups of the preceding step.

has coordinates ($\alpha = 173.05$, $\delta = 56.05$, $z = 0.0585$, [Lauer et al., 2014](#)).

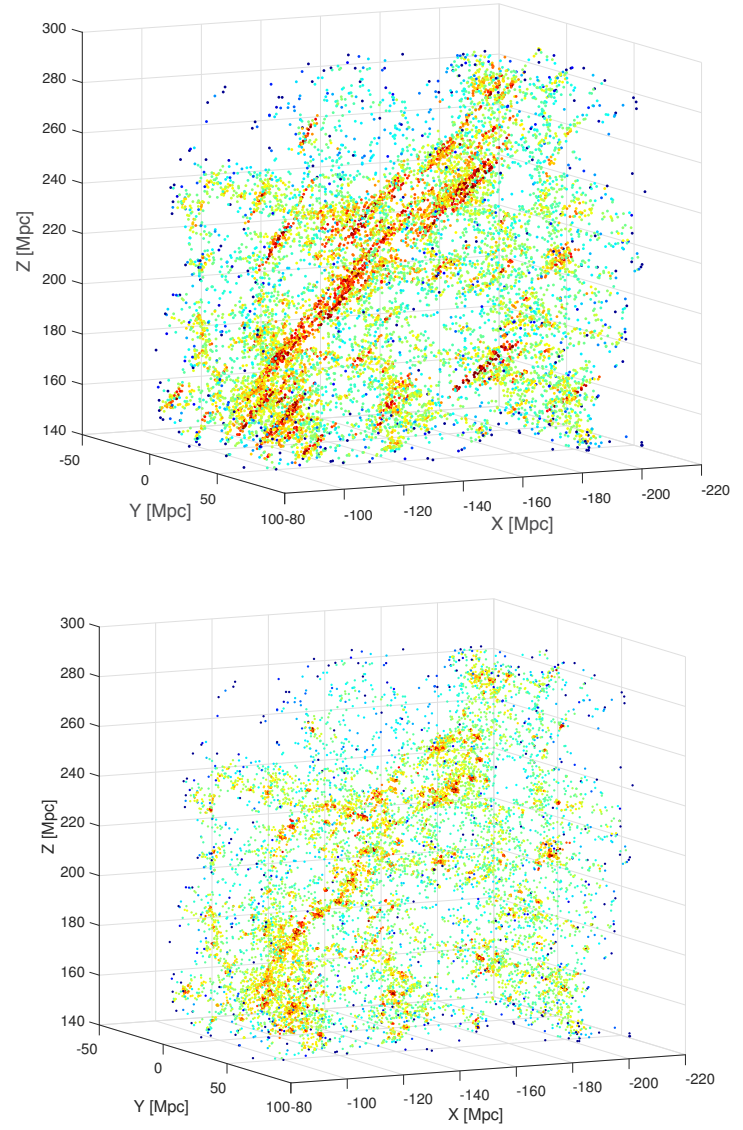


Fig. 5: 3D galaxies for the MSCC 310 supercluster volume. Top, galaxy positions before the application of the FoG correction. Bottom, Galaxy positions after correction for FoG effects. The color represent density as calculated from 3D VT. The highest density is represented in red while green to blue represents lower densities.

Finally, as described in section 4.2, we correct the D_C of the member galaxies in each system by re-scaling their dispersion range to the R_{vir} of the system. An example of the MSCC 310 volume, before and after the correction, is shown in Figure 5.

6.2. Application of GFIF to MSCC 310

With the co-moving distances for the MSCC 310 galaxies corrected for the FoG effect, we proceeded to transform their sky coordinates to rectangular ones following equations 1, 2 and 3.

The N_{gal} was now taken to be the total number of galaxies in the box of MSCC 310, $N = 12\,286$, for which we applied the GFIF method. The VT algorithm was then applied to calculate volumetric numerical densities. We used a segmentation parameter of $f = 16$ for the HC algorithm. From that, we identified

Table 3: Main properties of the 25 richest systems identified in the volume of the supercluster MSCC 310.

System Nr.	N_{mem}	RA_{J2000}	C_{BMG} Dec $_{J2000}$	z	RA_{J2000}	C_{FoG} Dec $_{J2000}$	z_{LOS}	σ_v [km s $^{-1}$]	R_h [h_{70}^{-1} Mpc]	R_{vir} [h_{70}^{-1} Mpc]	cross-ref ACO Nr.
(1)	(2)	(3)	(4)	(5)	(6)	(7)	(8)	(9)	(10)	(11)	(12)
1	123	173.09667	55.96744	0.0515	173.01489	56.09476	0.0535	1182	1.09	2.54	A1291A
2	103	174.01464	55.07526	0.0571	174.17793	55.19984	0.0587	1103	1.28	2.56	A1318A
3	95	180.26970	56.37019	0.0648	180.07048	56.20431	0.0649	762	1.04	1.87	A1436
4	94	167.09625	44.15030	0.0587	167.10957	44.07194	0.0590	644	0.81	1.53	A1169
5	91	176.83909	55.73018	0.0515	176.80652	55.69322	0.0518	712	0.80	1.64	A1377
6	82	177.19063	54.51936	0.0601	177.05852	54.64399	0.0604	845	0.95	1.94	A1383
7	67	168.84947	54.44412	0.0695	168.90590	54.50901	0.0700	659	0.91	1.63	
8	61	175.27722	55.18836	0.0593	175.25812	55.29493	0.0609	1103	1.30	2.58	A1349A
9	61	163.40237	54.86794	0.0716	163.54104	54.84312	0.0722	640	0.89	1.58	
10	59	172.33060	54.12608	0.0689	172.44575	54.08347	0.0690	582	0.75	1.40	A1270
11	54	158.24537	56.74813	0.0448	158.32527	56.82434	0.0454	459	0.69	1.16	
12	52	180.22849	51.42263	0.0666	180.46535	51.65240	0.0649	1069	1.08	2.37	A1452
13	50	152.32009	54.21099	0.0465	152.41409	54.42037	0.0460	415	0.68	1.08	
14	46	183.70265	59.90619	0.0600	183.59629	59.90299	0.0599	443	0.75	1.17	A1507B
15	43	168.06955	57.07599	0.0471	168.12753	57.04832	0.0467	491	0.77	1.26	
16	42	178.37743	52.68944	0.0716	178.59933	52.77017	0.0695	761	0.84	1.74	
17	39	151.21598	54.56786	0.0470	150.99614	54.65456	0.0472	460	0.64	1.13	
18	39	163.28303	56.33167	0.0772	163.35966	56.33847	0.0745	1003	0.89	2.13	
19	36	172.42861	55.38047	0.0685	172.44796	55.42240	0.0684	534	0.54	1.19	
20	36	162.94746	55.38567	0.0739	162.89992	55.34739	0.0737	367	0.68	1.00	A1112A
21	34	182.19381	53.33371	0.0813	182.19494	53.31805	0.0821	573	0.66	1.33	
22	33	181.31486	43.16902	0.0528	181.40583	43.20470	0.0526	504	0.67	1.23	
23	31	177.05076	52.85209	0.0503	177.04947	52.59945	0.0505	556	0.67	1.31	
24	31	178.57105	55.47082	0.0508	178.68334	55.20458	0.0513	584	0.82	1.45	
25	31	151.31217	53.14899	0.0463	151.31677	52.99140	0.0451	431	0.68	1.11	

Notes. The complete version of this table and the tables of systems of the other superclusters can be found in the electronic version of this paper.

768 low density groups and, for each pair, we calculated the D_E distance between centers and the BC weight. As expected, the implementation of the HC algorithm over all galaxies detected larger groups (~ 15 galaxies on average now) and more elongated, with a mean σ_j of $1.8 h_{70}^{-1}$ Mpc compared with the mean σ_j of $0.5 h_{70}^{-1}$ Mpc found with the application of GSyF.

In order to filter the connections, a linking length of $D_{max} = 8 h_{70}^{-1}$ Mpc was used resulting on 334 edges. As described above, D_{max} and f were obtained by the optimization process described in Santiago-Bautista et al. (2019). The second filter, the minimum mean linear density along the edge cylinders (in this case $0.008 \text{ gal.Mpc}^{-3}$), left 273 links from the 316 connections smaller than D_{max} . This resulted in 34 trees, to which we applied MST . Of these, only 9 are linking 3 or more systems of galaxies with a richness N_{mem} above 11 galaxies, the rest are isolated bridges and tendrils. This result is shown in the dendrogram depicted in Figure 6 (top panel) which shows 9 dominant filaments for the MSCC 310 supercluster.

Concerning the systems embedded in the structures, from the 359 HC groups (nodes) in the spanning trees, 116 matched with the systems with $N_{mem} \geq 10$ identified with GSyF. From these, 61 were found to be in filaments (53%), 26 (22%) in bridges between pairs of systems, and 29 (25%) not connected by bridges, that is, relatively isolated.

The filaments detected by the GFIF algorithm in the MSCC 310 supercluster and their main properties are listed in Table 4. Column 1 assigns a sequential number to the filament; column 2 lists the number of systems detected by GSyF linked by the filament; column 3 shows the number of galaxies attributed to the filament; columns 4 to 6 are the mean, min. and max. redshift of the filament; column 7 corresponds to the

mean number density inside the filament; column 8 is the mean transversal radius of the filament measured at $10 \times d$; columns 9 and 10 show the number of nodes that constitute the filament and the number of central skeleton nodes, respectively; column 11 is the length of the filament skeleton.

We can also observe the filaments inside the MSCC 310 volume in Figure 6 (bottom panel). In this panel the 9 filaments are plotted over the distribution of galaxies in a RA [deg] \times Z [Mpc] plane. This projection allows the recognition of structures both in one of the coordinates of the sky plane and depth. Filaments are depicted in colors, the same colors in both panels of this figure. Isolated bridges (that connect two systems alone, without forming a filament) are represented only in the bottom panel and by black lines. Tendrils are not represented to avoid crowding. The longest paths for the filament skeletons, that is, those that connect the farthest systems of each filament, range from 18 to $62 h_{70}^{-1}$ Mpc and connect up to 11 systems inside the MSCC 310 volume. Moreover, we measured the paths between pairs of systems chained together by bridges; such distances range from 5 to $24 h_{70}^{-1}$ Mpc.

7. Validation of the methods

7.1. Checking the identified systems of galaxies

In order to validate our GSyF algorithm we compared the list of identified systems to different cluster and group catalogs in the region of SDSS.

For MSCC 310, for instance, GSyF detected 122 systems with ten or more galaxies and another 113 systems with $5 \leq N_{mem} < 10$. A match was considered positive if the projected

Table 4: Main properties of the filaments extracted through GFIF for the supercluster MSCC 310.

Fil. ID (1)	N_{sfil} systems (2)	N_{gfil} gals. (3)	redshift [mean, min, max] (4)	(5)	(6)	d_{fil} [h_{70}^{-1} Mpc $^{-3}$] (7)	R_{fil} [h_{70}^{-1} Mpc] (8)	N_{nod} filament (9)	skeleton (10)	ℓ_{fil} [h_{70}^{-1} Mpc] (11)
MSCC 310-F1	10	499	0.0609	0.0518	0.0689	0.4180	2.81	18	11	61.6
MSCC 310-F2	8	523	0.0502	0.0443	0.0588	0.5210	2.84	22	11	51.8
MSCC 310-F3	7	407	0.0481	0.0427	0.0528	0.3486	2.50	19	10	49.0
MSCC 310-F4	8	313	0.0656	0.0585	0.0710	0.4263	2.46	14	10	59.0
MSCC 310-F5	7	325	0.0700	0.0642	0.0774	0.5303	2.60	13	7	47.6
MSCC 310-F6	6	243	0.0725	0.0651	0.0791	0.2986	1.97	12	9	39.3
MSCC 310-F7	4	219	0.0551	0.0479	0.0619	0.4062	2.76	7	5	20.7
MSCC 310-F8	4	164	0.0546	0.0485	0.0617	0.2118	2.22	9	7	33.7
MSCC 310-F9	4	124	0.0464	0.0437	0.0528	0.1464	1.13	9	6	17.9

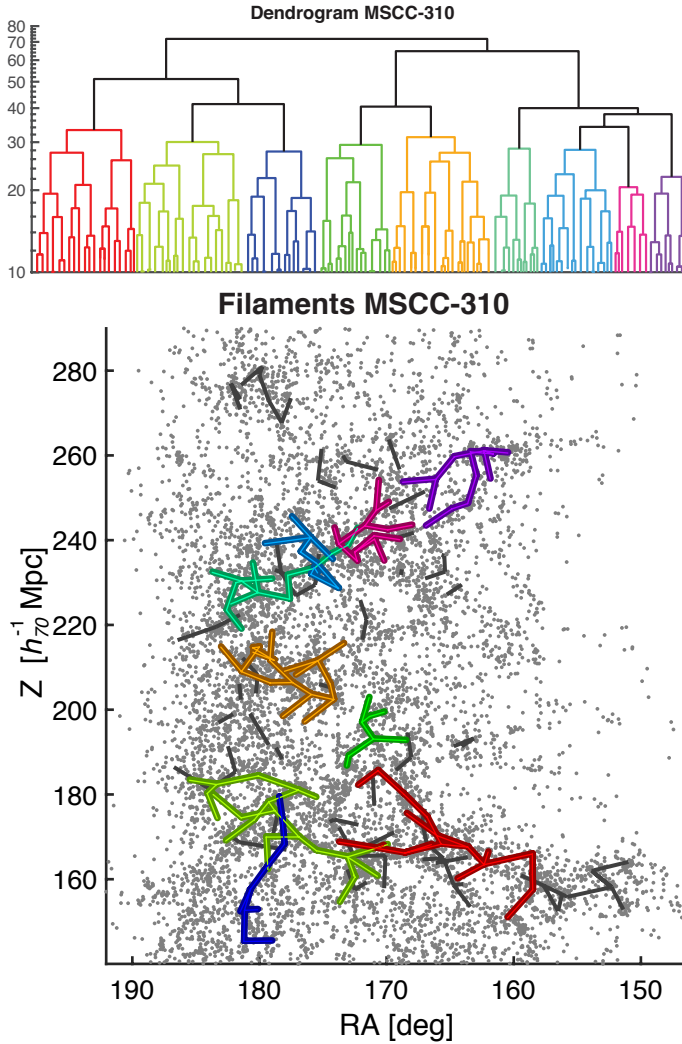


Fig. 6: Results of GFIF algorithm for the MSCC 310 supercluster volume. Upper panel: dendrogram with the 9 detected filaments represented by different colors. The y axis of the dendrogram plot indicates the distance at each level of the tree. Lower panel: RA \times Z distribution, where SDSS galaxies are represented by gray points and filaments are by lines according to the colors in the upper panel. Tendrils are represented by gray color lines.

positions of the system in the two compared catalogs were not

farther than $1 h_{70}^{-1}$ Mpc, while in redshift space we considered a difference $\Delta z = 0.007$ which corresponds to ± 200 km s $^{-1}$.

For the rich clusters, first we compared our results to the original Abell/ACO catalog (Abell et al., 1989), based on the most recent parameter measurements for its clusters (e.g. Chow-Martinez et al., 2014). Also, we compared the detected systems against the central galaxy position provided by the *Brightest Cluster Galaxy* catalog (Lauer et al., 2014, hereafter L14). Regarding catalogs based on the SDSS spectroscopic sample we compared with the C4 cluster catalog (Miller et al., 2005), based on the SDSS-DR2. For less rich clusters and groups we compared our systems with the *Multi-scale Probability Mapping clusters/groups* catalog (MSPM, Smith et al., 2012) and the Tempel et al. (2011) catalog (hereafter T11), carried over the SDSS-DR7 and -DR8 respectively. For the comparisons we used all systems detected by GSyF down to a richness of 5 galaxies.

By using the tolerance cylinder described above, 19 of the 37 Abell/ACO clusters inside the MSCC 310 box were detected as systems of richness above 5 galaxies with our method (51%), while the equivalent number was 26 (76%) for the 34 clusters in C4. There are 11 clusters in the L14 catalog embedded in the volume and 8 (73%) of them have GSyF counterparts. However, by increasing the aperture to $2 h_{70}^{-1}$ Mpc, we increased the detection of Abell clusters to 29/37 (78%), C4 clusters to 33/34 (97%) and L14 catalog to 100%, see Table 6. The increase of 20 – 30% in cluster matches by using a larger aperture size can be related to the fact that the mean separation of member galaxies increases for lower richness systems, and the determination of the cluster center then is subject to this separation, see Table 6. For example, A1452 and A1507 B have a GSyF counterpart located at $\sim 1.5 h_{70}^{-1}$ Mpc projected distance and $\Delta\sigma_v$ of ~ 630 km s $^{-1}$ and 120 km s $^{-1}$ respectively (See Table 3, systems No. 12 and 14), while their C4 counterparts are 0.7 and $0.4 h_{70}^{-1}$ Mpc away respectively.

Concerning the less massive systems, there are 315 groups detected by T11 and 213 groups listed in the MSPM catalog with richness larger or equal to 5 galaxies for the MSCC 310 volume. Our algorithm detected systems that correspond to 61% (79%) of the T11 groups and 67% (78%) of the MSPM groups, within an aperture of $1 h_{70}^{-1}$ Mpc ($2 h_{70}^{-1}$ Mpc) (see Table 6). This is acceptable for our purposes since we have constructed GSyF to find the clusters that present FoG effect, although we can clearly go farther towards poorer systems with it.

The region of the UMa supercluster has been previously studied by Krause et al. (2013). These authors identified 31 galaxy systems in the MSCC 310 area with a number of galaxies between 15 and 94 galaxies. We found that our GSyF sys-

Table 5: Glossary of parameters used by GSyF and GFIF algorithms

Param.	Description	MSCC 310
Properties of the rectangular box		
N	Total nr. of galaxies	12 286
V	Total volume	$(116 h_{70}^{-1} \text{ Mpc})^3$
$d = \frac{N}{V}$	Mean volumetric number density	$0.008 h_{70}^3 \text{ Mpc}^{-3}$
A	Projected area in the sky	$(12.65 \text{ deg})^2$
$d_{surf} = \frac{N}{A}$	Mean surface number density (sky projection)	76.9 deg^{-2}
v_i, a_i	Local volume or projected area of VT cell	each galaxy
d_i	Local VT (surface or volume) density	each galaxy
D_C	Comoving distance of the galaxy or system	each galaxy or system
D_E	Euclidean distance between two galaxies or two nodes (edge size)	each pair
D_{ske}	Euclidean distance of galaxy from filament skeleton	each galaxy
Amount of systems		
N_{Cl}	Richness of the supercluster (nr. of Abell/ACO clusters)	21
$N_{cut} = \frac{N_{gal}}{f}$	Nr. of extracted HC groups	1 140, 768
N_{HC}	Nr. of detected HC groups ($N_j \geq 3$) found by GSyF algorithm	1 015
N_{nodes}	Nr. of nodes found by GFIF algorithm which remained in the MSTrees	359
N_{FoG}	Nr. of systems (that survived the FoG filter)	255
N_{sys}	Nr. of systems with $N_{mem} > N_{min}$ in box which matched nodes	116
N_{sfil}	Nr. of systems embedded in the filaments	61
N_{spair}	Nr. of systems forming pairs connected by isolated bridges	26
N_{sout}	Nr. of systems not forming filaments or pairs	29
Amount of filaments, isolated bridges and tendrils		
N_{fil}	Nr. of filament candidates of the supercluster	4
N_{ske}	Nr. of detected filaments in the box (linked bridges)	9
N_{brid}	Nr. of detected isolated bridges between two systems only	17
N_{tend}	Nr. of detected tendrils (not bridges or filaments)	18
Properties of the systems		
$P_j(x)$	Gaussian model for detected HC group	each HC group
N_j	Richness the detected HC group	each HC group
C_j	Centroid position of the detected HC group	each HC group
σ_j	Compactness (covariance) of the detected HC group	each HC group
C_{BMG}	Position of Brightest HC group Member Galaxy	each HC group
C_{FoG}	Centroid position of the detected FoG system	each system
N_{mem}	Richness (nr. of galaxies) of the detected FoG system	each system
N_{min}	Minimum nr. of galaxies for systems in filaments at different z	10
R_h	Harmonic radius of the detected FoG system	each system
R_{vir}	Virial radius of the detected FoG system	each system
M_{vir}	Virial mass of the detected FoG system	each system
v_{LOS}	Robust line-of-sight velocity of the detected FoG system	each system
σ_v	Robust velocity dispersion of the detected FoG system	each system
Properties of the filaments		
N_{edges}	Nr. of edges that survived filter 1	334
N_{links}	Nr. of edges that survived filters 1 and 2	316
N_{trees}	Nr. of trees after MST	17
N_{nod}	Nr. of nodes in the filament (or in the skeleton)	each filament (skeleton)
ℓ_{fil}	Length of filament skeleton	each filament
R_{fil}	Mean radius of the filament	each filament
d_{fil}	Mean galaxy number density inside the filament	each filament
N_{gfil}	Nr. of galaxies hosted in the filaments of the box	2 568
V_{fil}	Volume occupied by the filaments of the box	$(1.16 h_{70}^{-1} \text{ Mpc})^3$
GSyF and GFIF parameters		
d_{bas}	Projected number density baseline	15.7 deg^{-2}
δ_i	Local density contrast	each galaxy
N_{gal}	Nr. of galaxies above the baseline d_{bas}	6 842
R_a, S_a, M_a	Parameters of iterative process for FoG correction	each HC group
f	Segmentation parameter (OPTIMIZATION)	6, 16
BC	Bhattacharyya coefficient (edge weight)	each edge
D_{max}	Linking length (first filter) (OPTIMIZATION)	$8 h_{70}^{-1} \text{ Mpc}$
d_{edge}	Edge cylinder density (second filter)	each edge
R_{cy}	Filament concentric cylinder radius	each filament

tems match with 24 (77%) of these clusters within an aperture of $3 h_{70}^{-1} \text{ Mpc}$, of which 10 are Abell clusters.

The systems detected in the main portion of the MSCC 310 supercluster are depicted on a sky projected distribution, in Figure 7 (top panel), by black circles with radius equal to the measured virial radius. The system positions from the Abell, C4, L14, MSPM and T11 catalogs are depicted respectively as red, pink, cyan, blue and green points. We also observe that

the system membership number detected by GSyF is in agreement, for most of the cases, with the number of members for the same systems detected by T11, C4 and MSPM (see Figure 8). Qualitatively one can observe in this figure that the richness from T11 is in better agreement with our measurements, while MSPM estimates a richness slightly lower than both ours and T11.

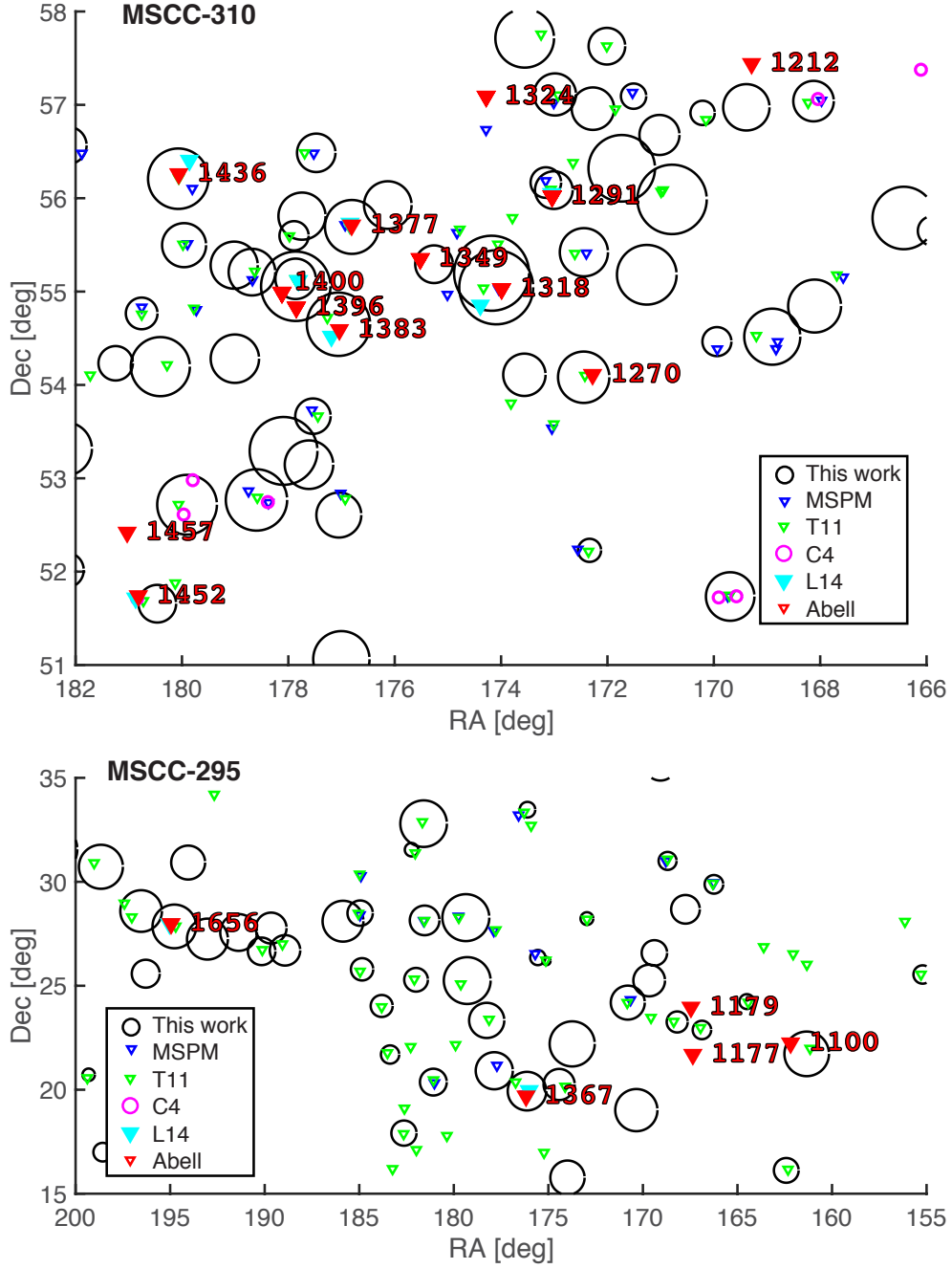


Fig. 7: Projected distribution in the sky of systems detected by GSyF. Top: Systems detected for the MSCC 310 (UMa supercluster). Bottom: Systems detected for the MSCC 295 (Coma supercluster). The system radii are shown as circles of $r = R_{vir}$. For comparisons, the position of systems reported by MSPM, T11, C4, L14 and Abell catalogs are depicted by color points: blue, green, pink, cyan and red, respectively.

A similar analysis can be done for the other superclusters in our sample. For example, for the *Coma* supercluster (MSCC 295, Figure 7, bottom panel), the GSyF algorithm detected, in total, 115 systems. Of these, we found that A1656, the richest one, is composed of 579 galaxies. The estimated virial radius and mass are, respectively, $1.96 h_{70}^{-1}$ Mpc and $7.7 \times 10^{14} M_{\odot}$. The second richest cluster, A1367, has 243 galaxies, while its radius and mass are, respectively, $1.73 h_{70}^{-1}$ Mpc and $5.3 \times 10^{14} M_{\odot}$. These estimations are in good agreement with those measured

by Rines et al. (2003). The complete catalog of systems for each volume is available online².

7.2. Checking the filament skeletons

We compared the filaments obtained using the GFIF algorithm for the MSCC 310 volume with those presented by Tempel et al. (2014) (hereafter, T14) as extracted from their Table 2. We transformed the T14 *survey coordinates* filament positions (see

² https://gitlab.com/iris.santiagob89/LSS_structures

Table 6: GSyF systems detected by other catalogs for the MSCC 310 supercluster.

Aperture = $1 h_{70}^{-1}$ Mpc						
Other catalog	Number	Fraction	Number	Fraction	separation	
	$N_{mem} > 5$		$N_{mem} > 10$		h_{70}^{-1} Mpc	$\Delta\sigma_v$
Abell	19/37	51%	17/37	46%	0.45	295
C4	26/34	76%	24/34	71%	0.43	100
L14	8/11	73%	8/11	73%	0.50	340
T11	192/315	61%	73/105	70%	0.33	230
MSPM	142/213	67%	63/79	80%	0.34	145

Aperture = $2 h_{70}^{-1}$ Mpc						
Other catalog	Number	Fraction	Number	Fraction	separation	
	$N_{mem} > 5$		$N_{mem} > 10$		h_{70}^{-1} Mpc	$\Delta\sigma_v$
Abell	29/37	78%	24/37	65%	0.82	300
C4	33/34	97%	32/34	94%	0.77	166
L14	11/11	100%	11/11	100%	0.80	430
T11	249/315	79%	85/105	81%	0.64	320
MSPM	167/213	78%	68/79	86%	0.55	193

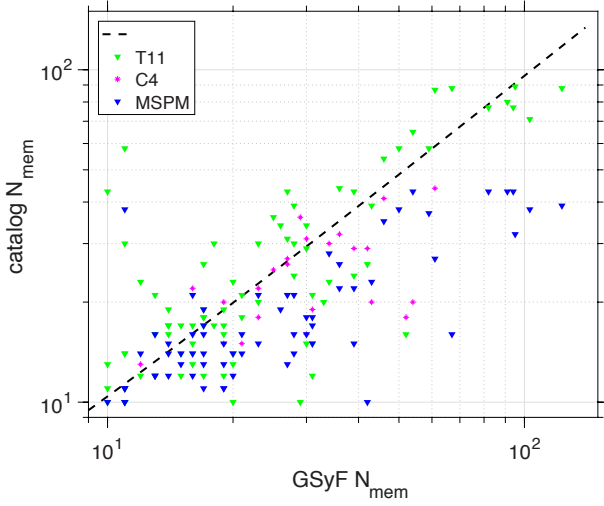


Fig. 8: Comparison of MSCC 310 supercluster GSyF system richness against the richness measured by other catalogs for the matching systems. Symbol colors are the same as the ones in Figure 7. The dashed line represents the identity.

T14, equation 1) to our rectangular space and cosmology. There are about 630 T14 filaments that lie in the sampled volume of MSCC 310 supercluster. These filaments have a mean length of $9 h_{70}^{-1}$ Mpc while the largest one has a length of $48 h_{70}^{-1}$ Mpc. As a comparison, the filament skeletons detected by GFiF have a mean length of $42 h_{70}^{-1}$ Mpc and the largest one has a length of $62 h_{70}^{-1}$ Mpc. We found 40% match between our detected filaments and T14 and 80% match with our isolated bridges and tendrils. The mean difference between the medial axis of T14 filaments matching the nearest filament/tendrill detected by us is $\sim 1.5 h_{70}^{-1}$ Mpc. T14 filaments are represented by a sequence of points forming a line. Then, the calculated separation was taken to be the distance from the T14 filament points to the edges of our filaments. Our filaments are depicted over T14 filaments in Figure 9. As can be seen, GFiF detects the most prominent (dense) filaments among the ones in T14.

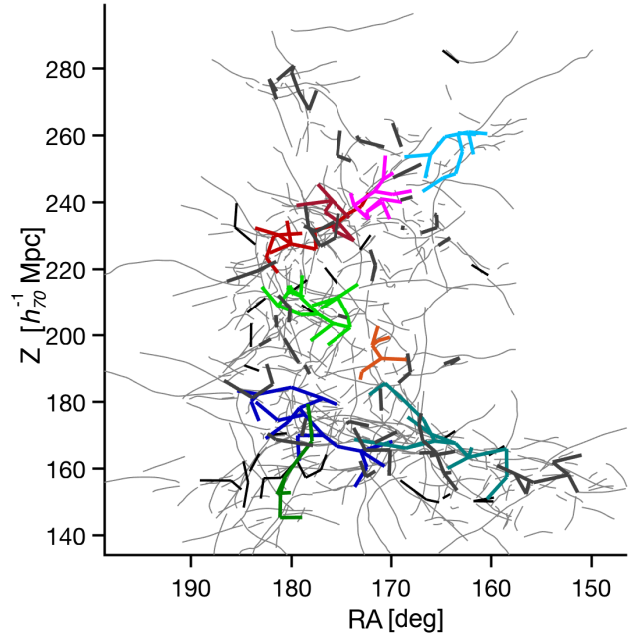


Fig. 9: Comparison of GFiF filaments for the MSCC 310 supercluster to the T14 filaments in the same region for the SDSS-DR8. Gray lines are T14 filaments. Colored lines depict filaments identified in this work.

7.3. Comparison with KDE density maps

Another test we did in order to validate the results from GSyF and GFiF algorithms was to apply an independent analysis to the galaxies in the MSCC 310 volume in order to corroborate the densities, nominally the *KDE* method, as described in section 3.6. A quantitative comparison in the space between the 3D *KDE* and the skeleton structures is left for upcoming works. Therefore, we restricted our analysis to 2D projections (density maps) of the 3D *KDE*, (XY, XZ, YZ). For this analysis we used kernels of size 1Σ (see section 3.6). Since each kernel is created based on the VT cell, we used d_{bas} as baseline density. We selected those regions for which $d_{kde} > d_{bas}$ in the

RA×Dec projected density map. Afterwards, we compared the position of the density peak of each region against the centroids of the 122 GSyF systems. We found that 93 GSyF systems with $N_j \geq 10$ (76%) match density peaks above $3 d_{bas}$. The remaining 29 GSyF systems (24%) are identified with density peaks in the range $(1 - 3) d_{bas}$. Moreover, we observe that the filament edges connect these density peaks forming chains of overdensity regions. In Figure 10 (top panel) we show the systems detected by GSyF represented by circles of $r = R_{vir}$ over the galaxy density distribution as measured using *KDE* in a RA×Dec projection. In the bottom panel of Figure 10 we show the filaments overlaid on the KDE density map for the MSCC 310 volume. The density maps are set in terms of the mean number density.

8. Filament Properties

8.1. Main properties of the filaments

In a similar way as described for MSCC 310, we applied the GFIF algorithm to the 46 superclusters of our sample, detecting a total of 144 filaments in 40 superclusters which are listed in Table 7. This table also lists the parameters used or measured by GFIF: column 2 notes the segmentation parameter f , while column 3 presents the number of detected *HC* groups in the supercluster box. Column 4 shows the linking length (D_{max}) used to connect *HC* groups. The process of filtering the connections can be followed through columns 5 to 10, which show, respectively, the number of detected edges, the number of filtered links, the number of trees detected after applying *MST* and the final number of filaments, N_{ske} , number of isolated bridges, N_{brid} , and tendrils, N_{tend} . Column 11 lists the minimum richness we considered for GSyF systems to be taken as ends of the bridges. Column 12 to 14 present, respectively, the fraction of these systems included in the GFIF filaments, in isolated bridges and the ones not connected by bridges. Finally, columns 15 to 17 show the number of galaxies hosted in the GFIF filaments, N_{gfil} , and the filling factors calculated as V_{fil}/V and N_{gfil}/N . The list of detected filaments for all studied supercluster volumes can be consulted in Table 8, in the same format as the one presented in Table 4. The MSCC 75, MSCC 76, MSCC 264, MSCC 441, MSCC 579 and MSCC 586 superclusters have not been evaluated with GFIF due to the sparseness of the SDSS coverage in these sky areas.

The filament skeletons detected by GFIF have lengths between 9 and $130 h_{70}^{-1}$ Mpc. Figure 11 depicts the length distribution for all the detected filaments. The distribution shows that the majority of the structure lengths range from 10 up to $40 h_{70}^{-1}$ Mpc. There are two structures longer than $100 h_{70}^{-1}$ Mpc. A $130 h_{70}^{-1}$ Mpc long filament is located in MSCC 323, containing the Abell clusters A1449 B and A1532 A, the second in MSCC 335, of $105 h_{70}^{-1}$ Mpc, containing A1478 A, A1480 B, and A1486 A. Excluding these two particular cases, we observe that the mean length of the filaments is about $37 h_{70}^{-1}$ Mpc while the median corresponds to $29 h_{70}^{-1}$ Mpc.

8.2. Distribution of galaxies along the filaments

In order to evaluate the environment within the filaments, we extracted longitudinal profiles of number density. In Figure 12 we show the longitudinal distribution of galaxies for all bridges, from one extreme to the other (ending systems), in the supercluster MSCC 310. We observe that the density of galaxies is higher near the ends of the bridges, as expected, and decreases

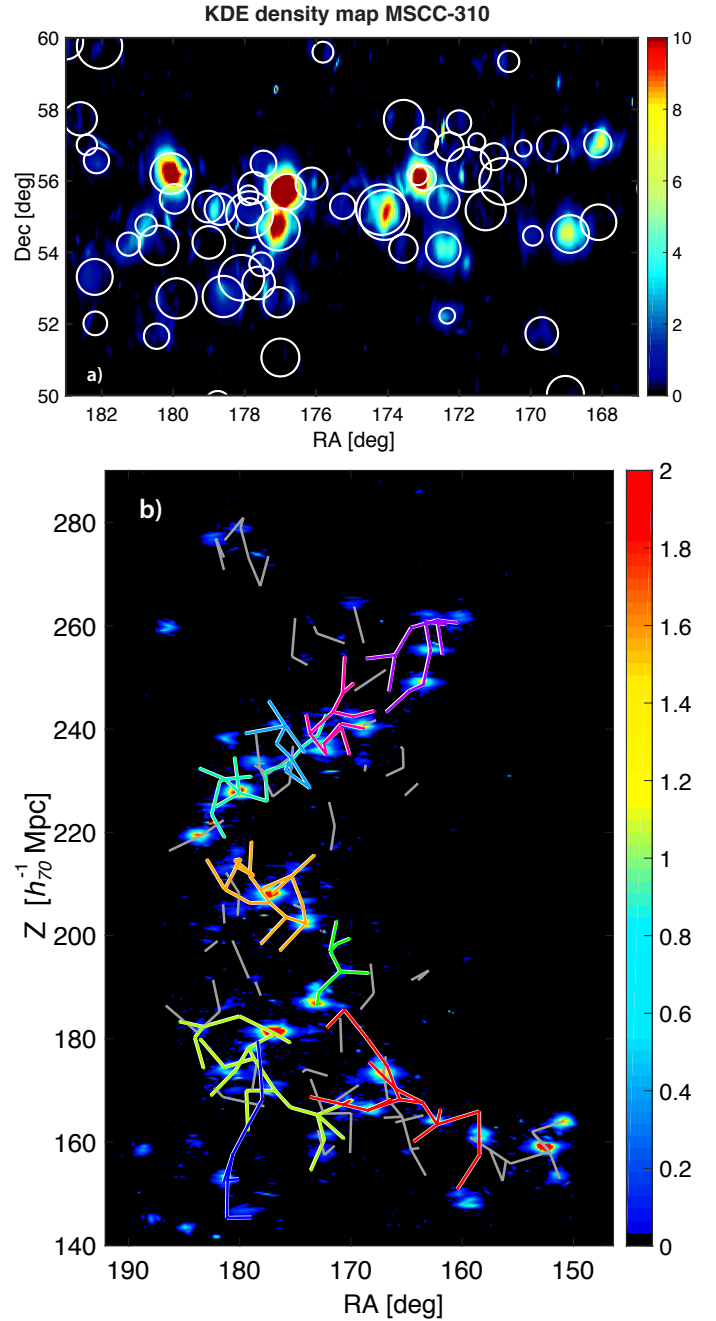


Fig. 10: (Top): RA×Dec. projected density map as measured from 3D-KDE with 1σ in terms of the density contrast. The GSyF systems are represented by white circles with radius scaled to the estimated R_{vir} . (Bottom): RA×Z projection. The filaments detected in this work are overlaid in color. Density is represented following the color scale displayed on the right, where denser regions are redder and less dense zones are bluer.

through the midpoint between systems. Then we proceed to extract density profiles for bridges, from the systems to the midpoint, by counting the galaxies that lie within a cylinder of radius $1 h_{70}^{-1}$ Mpc with medial skeleton set by the bridge skeleton. The galaxies are counted in slices of size $\Delta d = 0.5 h_{70}^{-1}$ Mpc along the skeleton axes. We also calculated the longitudinal profiles after excluding the galaxies belonging to systems (considered at $1.5 R_{vir}$) from their bridges, in order to determine pure filament profiles. These profiles allow to evaluate the mean density contrast

Table 7: Summary of the properties of the filaments detected by GFiF for the superclusters in Table 1.

MSCC ID	f	N_{cut}	D_{max}	N_{edges}	N_{links}	N_{trees}	N_{ske}	N_{brid}	N_{tend}	N_{min}	Fraction (%) of systems in			N_{gfil}	Filling factor (%)	
											filaments N_{sfil}/N_{sys}	bridges N_{spair}/N_{sys}	isolated N_{sout}/N_{sys}		V_{fil}/V	N_{gfil}/N
(1)	(2)	(3)	(4)	(5)	(6)	(7)	(8)	(9)	(10)	(11)	(12)	(13)	(14)	(15)	(16)	(17)
55	10	81	6	7	6	2	2	0	0	10	63.6	0.0	36.4	121	0.2	14.9
72	16	121	8	29	28	6	4	1	1	8	56.7	6.7	36.7	829	1.0	42.7
175	29	86	14	36	29	4	4	0	0	6	57.7	0.0	42.3	507	0.9	20.2
184	27	78	15	29	13	2	2	0	0	6	57.1	0.0	42.9	218	0.6	10.4
211	16	93	12	29	22	2	1	0	1	5	100.0	0.0	0.0	233	1.0	15.7
219	27	71	17	65	36	3	2	2	-1	5	72.2	22.2	5.6	279	1.1	14.6
222	15	124	16	84	43	5	2	0	3	4	44.4	0.0	55.6	97	0.2	5.2
223	15	52	18	31	19	2	1	0	1	4	75.0	0.0	25.0	11	0.1	1.4
229	16	116	19	93	44	8	1	1	6	4	37.5	25.0	37.5	32	0.1	1.7
236	32	270	9	124	94	11	7	2	2	18	55.3	8.5	36.2	1600	0.8	18.5
238	26	320	18	215	115	20	6	3	11	6	39.0	10.2	50.8	544	0.4	6.5
248	21	60	20	47	20	3	1	0	2	5	50.0	0.0	50.0	159	0.9	12.6
266	22	44	16	20	12	1	1	0	0	5	71.4	0.0	28.6	132	0.7	13.8
272	16	86	6	14	14	3	2	0	1	8	90.0	0.0	10.0	453	0.9	32.8
277	15	183	11	77	62	6	2	0	4	5	62.5	0.0	37.5	611	1.0	22.2
278	16	495	7	378	256	20	5	1	14	19	58.1	4.7	37.2	2144	1.6	27.1
283	23	101	16	32	21	5	3	0	2	4	44.4	0.0	55.6	263	0.5	11.3
295	14	1022	5	478	398	38	4	5	29	26	43.1	19.6	37.3	2992	1.0	20.9
310	16	768	8	334	273	34	9	7	18	10	52.7	12.7	34.5	2817	1.0	22.9
311	25	211	10	49	37	5	4	0	1	7	43.6	0.0	56.4	1118	0.8	21.2
314	14	40	8	13	7	2	2	0	0	7	50.0	0.0	50.0	112	0.7	20.1
317	15	56	17	56	31	3	2	1	0	5	61.5	15.4	23.1	63	0.5	7.5
323	22	151	16	46	29	5	2	2	1	4	26.3	10.5	63.2	239	0.5	7.2
333	19	104	11	39	28	6	3	1	2	7	45.8	8.3	45.8	282	0.6	14.3
335	23	135	13	108	65	8	3	0	5	8	52.9	0.0	47.1	478	1.1	15.4
343	11	244	7	51	33	5	3	1	1	7	34.5	6.9	58.6	335	0.4	12.5
360	38	58	20	54	23	4	3	0	1	6	47.6	0.0	52.4	218	0.8	9.9
386	9	362	7	165	120	20	4	2	14	9	60.6	12.1	27.3	636	0.7	19.5
407	16	70	18	49	20	3	1	0	2	4	50.0	0.0	50.0	101	0.7	9.0
414	9	1211	6	462	386	47	15	12	20	9	42.4	16.7	41.0	2232	0.8	20.5
419	15	115	11	39	22	5	3	3	-1	5	28.6	17.1	54.3	254	0.3	14.7
422	18	59	19	35	10	1	1	0	0	4	37.5	0.0	62.5	11	0.0	1.0
430	20	80	12	35	22	5	4	1	0	6	58.3	8.3	33.3	186	0.5	11.6
440	15	229	10	56	36	8	1	2	5	5	20.7	13.8	65.5	184	0.2	5.3
454	15	380	6	164	117	15	5	4	6	13	45.9	13.1	41.0	1516	1.2	26.6
457	21	194	9	80	68	7	6	0	1	8	66.7	0.0	33.3	1525	1.9	37.5
460	22	159	14	102	65	6	4	1	1	5	65.9	4.5	29.5	895	1.4	25.6
463	16	529	8	230	183	27	11	8	8	8	47.2	12.8	40.0	2228	1.1	26.3
474	15	495	5	245	209	20	7	3	10	16	48.0	12.0	40.0	1918	0.9	25.8
484	22	60	16	13	9	1	1	0	0	4	44.4	0.0	55.6	109	0.6	8.3

of the filaments as compared with the background density. In Figure 13 we show the longitudinal number density profile for all filaments detected in our sample. The stacked longitudinal profile including galaxies in systems is depicted by a blue line. The dispersion about the stacked profile is represented by a blue shaded area. The pure profiles (excluding the systems' galaxies) is represented by the red line, and its corresponding dispersion by a red shaded area. As can be seen, the mean density contrast along the filament is ~ 10 , that is, the filament is about 10 times denser than background.

8.3. Transversal density profiles

For the calculation of transversal density profiles, we excluded the galaxies located in systems, within a radius of $1.5 R_{vir}$. The density profile is calculated as described in section 3.7. The cylinder radius R_{cy} was set from 0 up to $10 h_{70}^{-1}$ Mpc in steps of $\Delta R_{cy} = 0.5 h_{70}^{-1}$ Mpc.

We computed the galaxy number density profile for filaments in two ways. First we counted the number of galaxies within concentric cylinders and divided them by the volume within the cylinders. We call this the local number density profile. For the second, we employed the number densities calculated using the $VT d_i$, as described in Sec. 3.1. Then we measure the mean VT number density within concentric cylinders. The local number density and VT number density profiles are scaled in density contrast and stacked together. Figure 14 shows the stacked profile for all filaments detected by GFiF, respectively for local densities (top panel) and VT densities (bottom panel). The first aspect to note is that local number density profiles are smoother although, in general, both mean profiles are similar. We can observe, in both local and VT density profiles, that overdensity extends up to $5 h_{70}^{-1}$ Mpc. At about $3 h_{70}^{-1}$ Mpc, the overdensity reaches a value around 3, while the typical characteristic density contrast of 10 is reached closer to $2 h_{70}^{-1}$ Mpc.

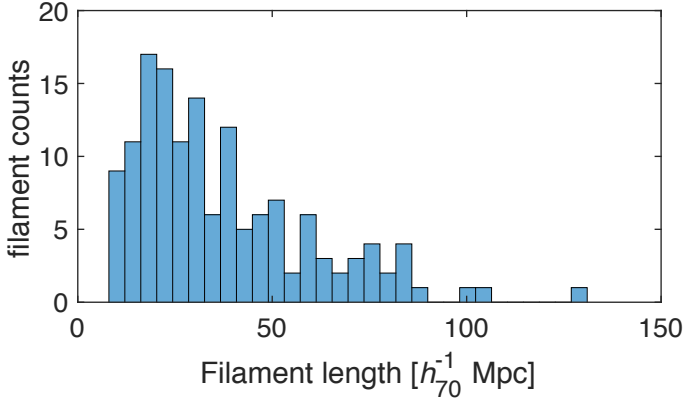


Fig. 11: Distribution of filament skeleton length for the 144 filaments detected by GFIF. The length used corresponds to the longest path between the systems at the extremity of the filament. See Table 8.

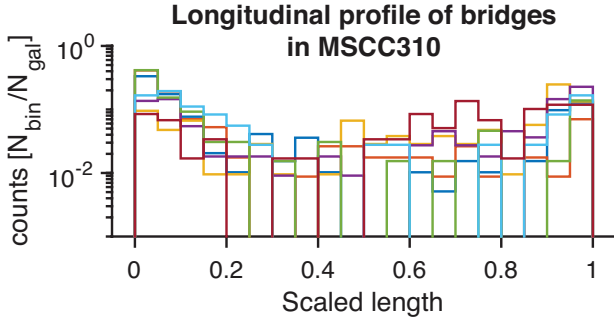


Fig. 12: Distribution of galaxies along bridges connecting pairs of systems for the nine MSCC 310 filaments. All bridges are scaled to length 1.0

Finally, we use the density profiles to estimate the mean radius of the filaments R_{fil} . This was achieved by considering the intersection point at which the local density profile crosses the $10 \times d$ line, as indicated in Figure 14 by the black solid line. The mean radius as well as the mean density of each filament is noted in Table 8.

Figure 15 (top panel) presents the radii distribution for all the filaments. The filament radii range from 0.6 to $4.5 h_{70}^{-1}$ Mpc with a mean value of $2.4 h_{70}^{-1}$ Mpc. The bottom panel of the figure depicts the filament radius as a function of the filament length. We observe that the filament length does not correlate with the filament radius. However, it is important to note that the radius varies slightly around the mean value along the filament path.

9. Properties of galaxies in filaments

9.1. Stellar mass profile

We constructed a galaxy stellar mass profile for all filaments by using the masses from MPA-JHU group (Brinchmann et al., 2004; Kauffmann et al., 2003; Tremonti et al., 2004) described in Section 2.2. First, we weighted the mass by the average mass of the volume under analysis to remove the redshift dependence of the stellar mass (Chen et al., 2017). This weighting is equivalent to a normalization of the stellar mass and allows to carry out a

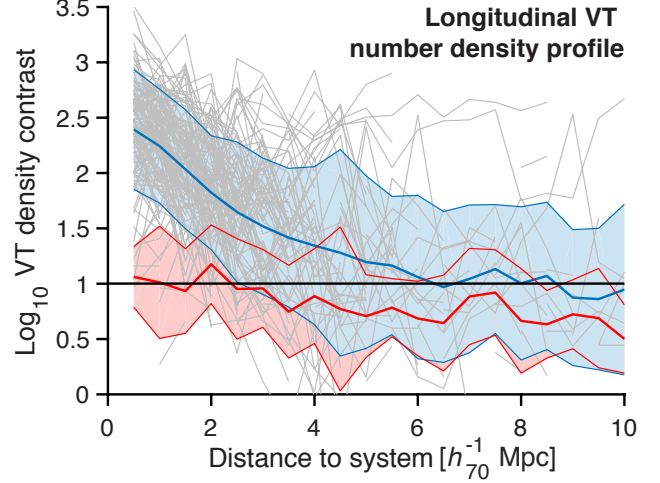


Fig. 13: Longitudinal VT density distribution for galaxies in all bridges of filaments detected by GFIF. Profiles are considered from the system center to the middle of the bridge. The thick blue line depicts the mean longitudinal profile for bridges including galaxies in systems. The thick red line corresponds to the mean longitudinal profile for all filaments excluding galaxies belonging to systems within $1.5 R_{vir}$. Blue and red shaded areas are the dispersion about the stacked profile.

stacking procedure in order to increase the signal of the profiles. This mass profile is extracted as described in Section 3.7.

Figure 16 shows the stacked stellar mass profile for all filaments. The variance of the stacked profile is depicted by the error bars. We observe that, statistically, the stellar masses of the filament galaxies are larger than the average mass up to about $2 h_{70}^{-1}$ Mpc, while beyond $3 h_{70}^{-1}$ Mpc they tend to be 10% smaller. This region farther than $3 h_{70}^{-1}$ Mpc probably represents the dispersed population of the supercluster, associated to the more extended sheet component. Thus, our results indicate that the stellar mass correlates with the distance to the filament skeleton, being larger (up to 25%) near the skeleton than far from it. These results are in good agreement with the results presented by Chen et al. (2017) for MGS sample from DR7 (Abazajian et al., 2009). Our results are also compatible with those presented by Alpaslan et al. (2016) and Kraljic et al. (2018), for the GAMA spectroscopic survey, who find similar trends for the filaments found at redshifts $z < 0.09$ and $0.03 \leq z \leq 0.25$, respectively.

9.2. Morphological type

In order to analyze if there is some morphological trend in the population of filament galaxies (as may be expected from the morphology-density relation), we also constructed morphology profiles based on morphological classifications by Huertas-Company et al. (2011). They classify the galaxies in four morphological types. For our analysis we used the probability $p(\text{Early}) = p(E) + p(S0)$ that classifies galaxies in early type as $p(\text{Early}) > 0.5$ and late type as $p(\text{Early}) < 0.5$. Then we computed the distribution of both galaxy types as a function of the distance to the filament skeleton. The distributions were normalized so they can be compared and stacked for all filaments in our sample in a similar way as a profile extraction, again excluding galaxies in systems. The result is shown in Figure 17.

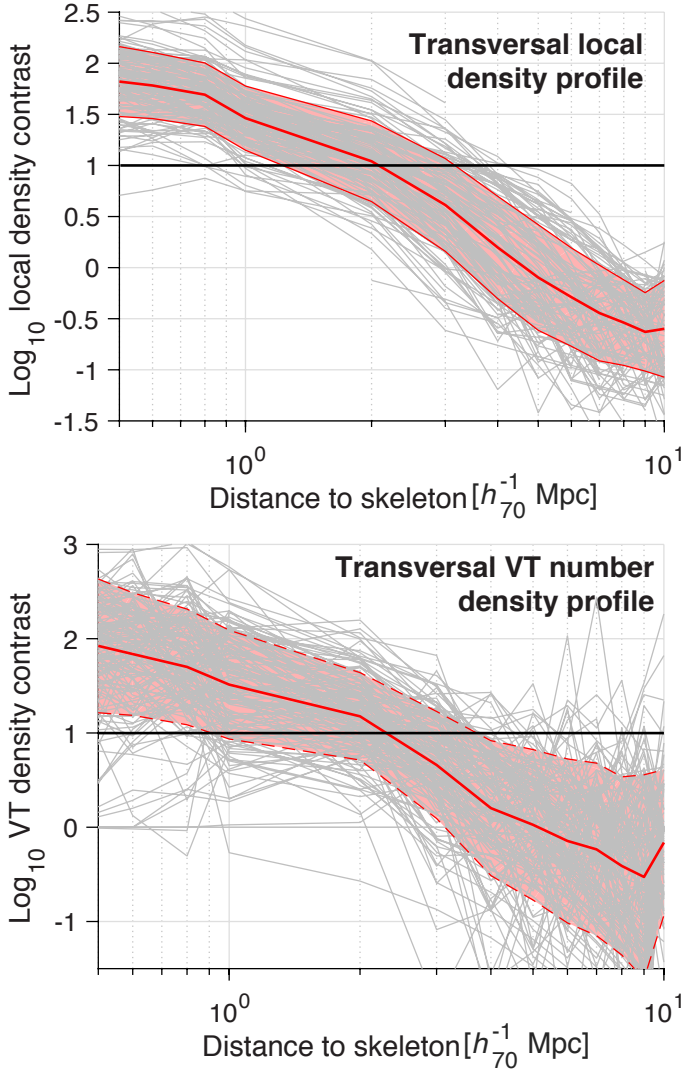


Fig. 14: Stacked number density profiles for the 144 filaments identified by GFIF. Individual profiles are represented by thin gray lines. Top: The red lines corresponds to the mean local density (stacked) profile. Bottom: Mean VT density stacked profile. The solid line indicates the mean profile while the shaded area represents the dispersion of the profile. Solid black line depicts the density contrast of $10 \times d$.

Our results show that the fraction of early type galaxies is higher than the one for late types near the filament skeleton up to $\sim 2 h_{70}^{-1}$ Mpc. This effect is more notorious when computed as an early to late type ratio (Figure 17, bottom panel). We observe that at distances smaller than $2 h_{70}^{-1}$ Mpc, the fraction of early types reaches almost twice the fraction of late types. At larger distances (that is, towards the dispersed supercluster population) the fractions tend to be similar (E/S ratio ~ 1). A two sample Kolmogorov-Smirnov test applied to the distributions of early and late types in Fig. 17 reveals that, for the first bins, they are significantly different (p-value lower than 0.1). Our results are consistent with those presented by Kuutma et al. (2017) for the Huertas-Company et al. (2011) sample – they also observe that early type galaxies are more abundant near the filament skeleton.

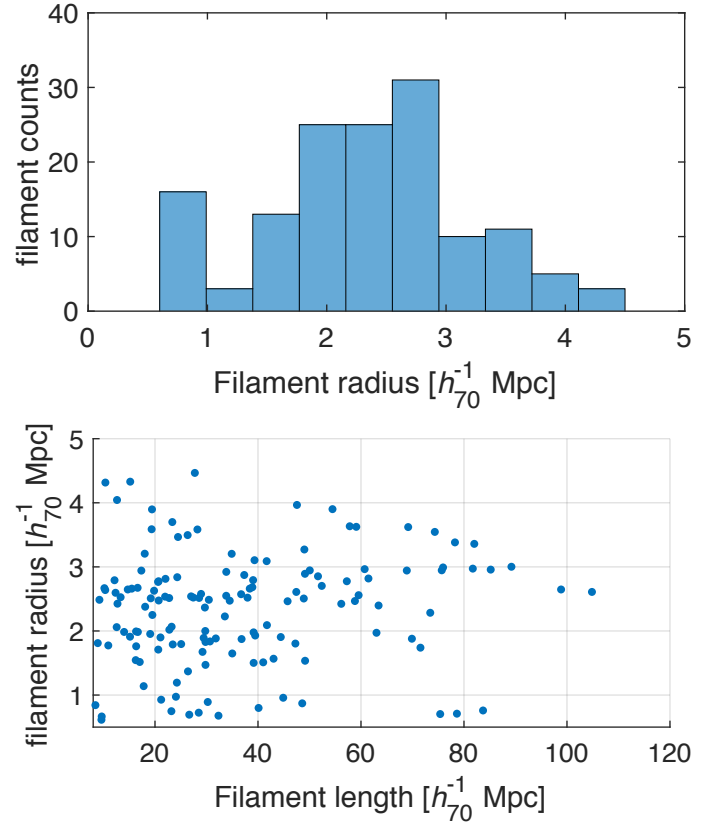


Fig. 15: Top: distribution of radius of filaments in our sample. Bottom, Comparison of filament length and radius for the 144 filaments detected by GFIF. The length used corresponds to the longest path between a pair of systems, that is, the skeleton length. See Table 8.

9.3. Activity type

For the analysis with respect to activity type, we used the activity classification from the MPA-JHU group, (Brinchmann et al., 2004; Kauffmann et al., 2003; Tremonti et al., 2004) described

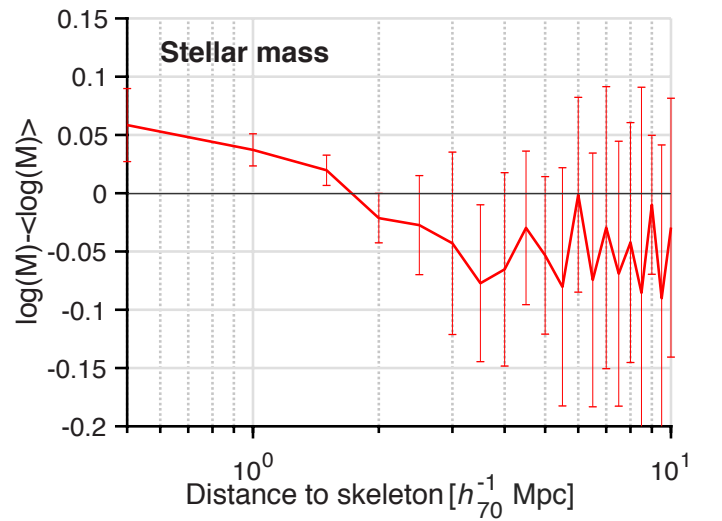


Fig. 16: Stacked transversal stellar mass profile for the 144 filaments detected by GFIF. Errors correspond to the variance of the stacked profiles.

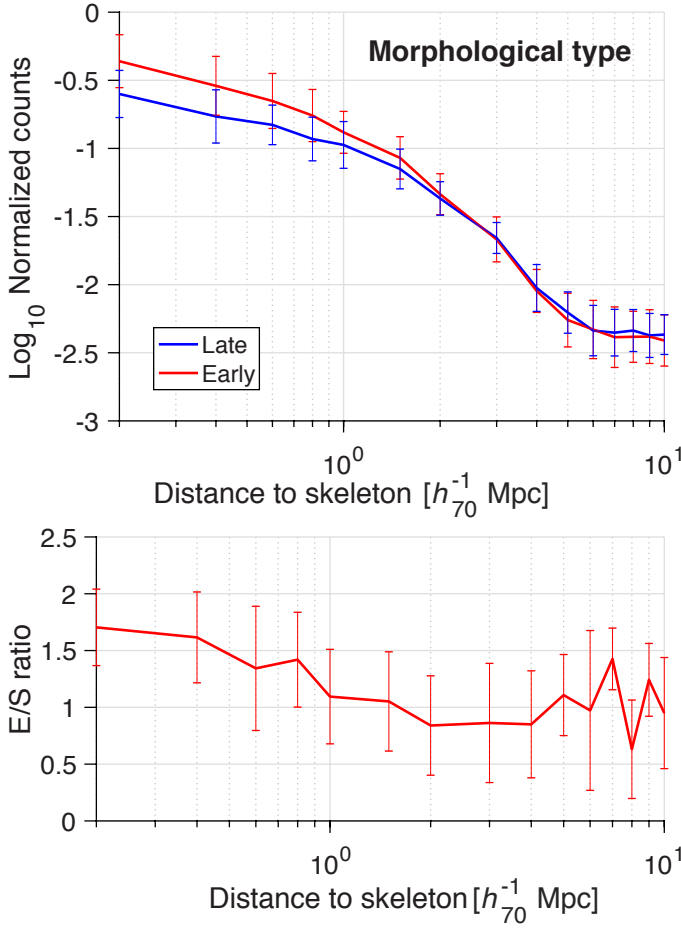


Fig. 17: Top: stacked transversal morphological type profiles for the 144 filaments detected by GFIF. The error bars correspond to the variance of the stacked profiles. Bottom: early-late type ratio as function of the distance to the filament skeleton.

in Section 2.2. We computed the distribution of the different galaxy activity populations as a function of the filament skeleton distance. All distributions are normalized for all filaments and stacked together.

Figure 18 divides galaxies into four activity groups: AGNs, SF galaxies, LINERs and non-active galaxies (unclassified). The error bars were not displayed over the lines for clarity – note that they are very large, implying that we have to interpret this figure with caution. Another effect to take into account is that the fractions are averaged over all the filaments (at different redshifts). The most evident tendency we can see in these distributions is a decrease in the activity as long as the galaxies “approach” the filament, although the fractions for the dispersed component are very noisy. Inside the filaments, the tendency is to have more passive galaxies, implying again smaller fractions of AGNs and SF galaxies. However, the fraction of LINERs also increases towards the filament skeletons, possibly indicating a post-activity phase for the galaxies. Deeper analyses are necessary to give a clear picture of the effect of the filament environment on the activity of galaxies.

10. Conclusions

In this paper we studied the bridges and filaments of galaxies in the environment of superclusters of galaxies. We developed

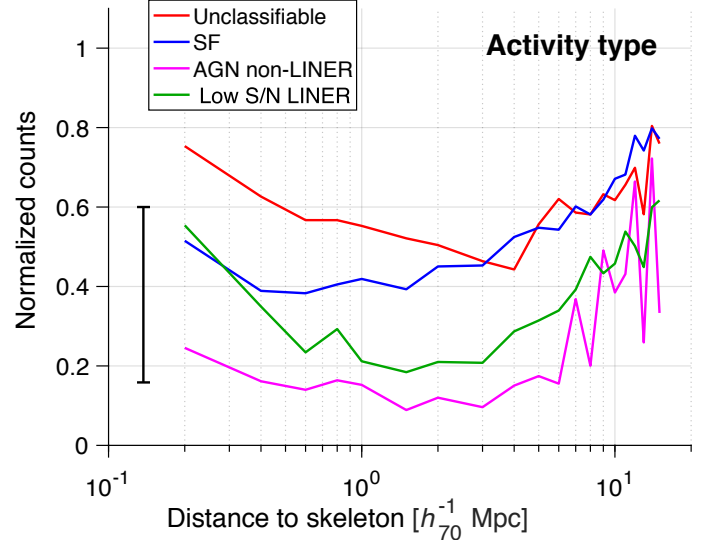


Fig. 18: Stacked transversal activity type profiles for the 144 filaments detected by GFIF. The black bar on the left represents the typical errors on the stacked profiles, not overlaid for clarity.

two algorithms, the *Galaxy Systems-Finding* algorithm, GSyF, and the *Galaxy Filaments-Finding* algorithm, GFIF, respectively to detect systems of galaxies (clusters and groups), aiming especially to correct for the finger-of-God effect, and to identify the elongated structures just mentioned. These algorithms were applied to a sample of SDSS galaxies with spectroscopic redshifts in rectangular boxes enclosing 46 superclusters of galaxies selected from MSCC catalog in a redshift range from 0.02 to 0.15.

GSyF and GFIF employ a set of different classic pattern recognition methods. Both of them are probabilistic in the sense that they define systems and filaments as a function of the relative position and orientation of the Gaussian groups, which are detected with a *Hierarchical Clusterization* method. For GSyF, the membership of the Gaussian groups is refined by using a virial approximation, allowing to discern gravitationally bound systems of galaxies from misdetections. For GFIF, these measurements are used to define a general tree from which we extract independent structures based on density criteria. Although the *HC* algorithm needs to be optimized for the number of clustering groups, this can be automatized based on the density function characterizing the survey. The structures are represented by a filament skeleton that allows to measure and trace quantitatively the filament path.

We show (section 7.1) that the systems detected by our methodology are in good agreement with those reported in the literature. Specifically, our comparisons of the systems sample against other cluster and group catalogs (Abell, C4, L14, T11 and MSPM) showed a match rate above 78% for groups with richness above 5 galaxies at redshifts $z < 0.11$. For systems with richness above 10 galaxies the coincidences were slightly higher for the group catalogues (T11 and MSPM) and slightly lower for the cluster catalogues (Abell and C4). Moreover, the richness, velocity dispersion and virial radius of systems measured by the GSyF algorithm are in good agreement with those reported in other system catalogs. Our GSyF algorithm detected a total of 2 705 systems in the rectangular boxes enclosing the volumes of 45 of the superclusters in our sample. Of these, 159 systems with

richness above 10 galaxies were not previously reported in the literature³.

We also compared, in section 7.2, the results of our filaments-finding algorithm with those of Tempel et al. (2014) for the same regions. We observe that T14 filaments are shorter, more numerous and describe sparser and finer structures while GFIF detects larger and denser elongated structures that bridge galaxy systems. Our filaments, in some sense, link several T14 threads in one larger structure, providing a broader picture of the filament. The comparison with isolated bridges and tendrils (a sub-product of our algorithm) shows a match of 80% with T14 filaments and comparable filament lengths.

The GFIF algorithm detected a total of 144 filaments and 63 isolated bridges in the rectangular boxes enclosing the volumes of 40 of the superclusters in our sample. The supercluster filaments we detected have lengths from 9 up to $130 h_{70}^{-1}$ Mpc (mean $37 h_{70}^{-1}$ Mpc, median $29 h_{70}^{-1}$ Mpc) while the isolated bridges have lengths between 5 and $15 h_{70}^{-1}$ Mpc. These values are consistent with the median bridge length value from Kraljic et al. (2019), $7.9 h_{70}^{-1}$ Mpc, for the HORIZON-AGN simulation.

For most of the cases, the numerical density inside the filaments was found to be between 5-15 times the mean density. The radii of the filament skeletons range from 0.6 up to $4.5 h_{70}^{-1}$ Mpc, with most between 2 and $3 h_{70}^{-1}$ Mpc. These values are consistent with the ones found by Cautun et al. (2013) by applying the NEXUS algorithm to an N-body simulation.

We also compared the properties of the galaxies that inhabit the filament as a function of the distance from its skeleton. We conclude the following: i) The transversal local and VT number density profiles for pure filaments show that, at distances up to $5 h_{70}^{-1}$ Mpc, the filaments have a positive overdensity respect to the background density inside the boxes. ii) At distances of about $3 h_{70}^{-1}$ Mpc, the density contrast reaches a value of 3, a limit that matches the range where typically the environmental effects studied in section 9 seem to apply. iii) The mean density contrast of the filaments, 10, is reached closer to $2 h_{70}^{-1}$ Mpc, a limit that we used as reference for estimating the radius of the filaments.

Our analysis regarding the stellar masses, morphological type and activity type show correlations between these galaxy properties and the distance from the filament skeleton. We arrive to the following conclusions: i) Inside $3 h_{70}^{-1}$ Mpc from the filament skeleton the galaxy stellar masses increase up to about 25%. This result leads to two hypotheses: (a) the mass growth of the galaxies is sensitive to the environment, or (b) the dynamical evolution brings massive galaxies into the potential well of the filaments. This result confirms several analyses which suggest that stellar masses are sensitive to the environment (Alpaslan et al., 2015, 2016; Poudel et al., 2016; Chen et al., 2017; Malavasi et al., 2017; Kraljic et al., 2018; Musso et al., 2018). ii) The early to late type galaxy ratio has its maximum at the center of the filament and remains above ratio 1:1 up to a distance of $1.5 h_{70}^{-1}$ Mpc. This result is in good agreement with a similar work by Kuutma et al. (2017) for the SDSS. iii) Concerning the activity type, we observed that the fraction of AGNs and SF galaxies seem to be higher outside the filaments (in the supercluster dispersed component), showing a decrease as the galaxies approach these structures. Inside the filaments, the fractions of non-active galaxies and LINERs increase, indicating a possible post-activity phase. A similar result for the star-forming galaxies has been observed by Kraljic et al. (2018), for the GAMA spectroscopic survey.

The GSYF and GFIF algorithms can be used to search for this kind of structures in different surveys, using spectroscopic or photometric redshifts. We plan to apply them to other galaxy databases, like the ones that are becoming available for the southern celestial hemisphere, and also, to galaxy surveys that reach deeper redshifts. Both algorithms and catalogs can be obtained electronically upon request.

Acknowledgements. I.S.-B. thanks CONACyT and DAIP for funding this research. This project was partially financed by DAIP funding CIIC 205/2019. The authors are grateful to the anonymous referee for the important comments that helped to improve the paper. All the pattern recognition computing, statistics and graphics have been made using MATLAB®. Part of this work was carried out with the computational facility TITAN at the Institut de Recherche en Astrophysique et Planétologie, Toulouse, France. This work has made use of NASA's Astrophysics Data System Bibliographic Services. Funding for SDSS-III has been provided by the Alfred P. Sloan Foundation, the Participating Institutions, the National Science Foundation, and the U.S. Department of Energy Office of Science. The SDSS-III web site is <http://www.sdss3.org/>. SDSS-III is managed by the Astrophysical Research Consortium for the Participating Institutions of the SDSS-III Collaboration including the University of Arizona, the Brazilian Participation Group, Brookhaven National Laboratory, Carnegie Mellon University, University of Florida, the French Participation Group, the German Participation Group, Harvard University, the Instituto de Astrofísica de Canarias, the Michigan State/Notre Dame/JINA Participation Group, Johns Hopkins University, Lawrence Berkeley National Laboratory, Max Planck Institute for Astrophysics, Max Planck Institute for Extraterrestrial Physics, New Mexico State University, New York University, Ohio State University, Pennsylvania State University, University of Portsmouth, Princeton University, the Spanish Participation Group, University of Tokyo, University of Utah, Vanderbilt University, University of Virginia, University of Washington, and Yale University.

References

- Abazajian, K. N., Adelman-McCarthy, J. K., Agüeros, M. A., et al. 2009, *ApJS*, 182, 543
- Abell, G. O. 1961, *AJ*, 66, 607
- Abell, G. O., Corwin, Jr., H. G., & Olowin, R. P. 1989, *ApJS*, 70, 1
- Aihara, H., Allende Prieto, C., An, D., et al. 2011, *ApJS*, 193, 29
- Alam, S., Albareti, F. D., Allende Prieto, C., et al. 2015, *ApJS*, 219, 12
- Albareti, F. D., Allende Prieto, C., Almeida, A., et al. 2017, *The Astrophysical Journal Supplement Series*, 233, 25
- Alpaslan, M., Driver, S., Robotham, A. S. G., et al. 2015, *MNRAS*, 451, 3249
- Alpaslan, M., Grootes, M., Marcum, P. M., et al. 2016, *MNRAS*, 457, 2287
- Alpaslan, M., Robotham, A. S. G., Obreschkow, D., et al. 2014, *MNRAS*, 440, L106
- Alvarez, G. E., Randall, S. W., Bourdin, H., Jones, C., & Holley-Bockelmann, K. 2018
- Aragón-Calvo, M. A., Jones, B. J. T., van de Weygaert, R., & van der Hulst, J. M. 2007, *A&A*, 474, 315
- Aragón-Calvo, M. A., Platen, E., van de Weygaert, R., & Szalay, A. S. 2010, *ApJ*, 723, 364
- Beers, T. C., Flynn, K., & Gebhardt, K. 1990, *AJ*, 100, 32
- Biviano, A., Murante, G., Borgani, S., et al. 2006, *A&A*, 456, 23
- Bolton, A. S., Schlegel, D. J., Aubourg, É., et al. 2012, *AJ*, 144, 144
- Bond, J. R., Kofman, L., & Pogossyan, D. 1996, *Nature*, 380, 603
- Bond, J. R. & Szalay, A. S. 1983, *ApJ*, 274, 443
- Bond, N. A., Strauss, M. A., & Cen, R. 2010, *MNRAS*, 409, 156
- Brinchmann, J., Charlot, S., White, S. D. M., et al. 2004, *MNRAS*, 351, 1151
- Cautun, M., van de Weygaert, R., & Jones, B. J. T. 2013, *MNRAS*, 429, 1286
- Cen, R. & Ostriker, J. P. 1999, *ApJ*, 514, 1
- Chen, Y.-C., Ho, S., Brinkmann, J., et al. 2016, *MNRAS*, 461, 3896
- Chen, Y.-C., Ho, S., Freeman, P. E., Genovese, C. R., & Wasserman, L. 2015, *MNRAS*, 454, 1140
- Chen, Y.-C., Ho, S., Mandelbaum, R., et al. 2017, *MNRAS*, 466, 1880
- Chow-Martinez, M., Andernach, H., Caretta, C. A., & Trejo-Alonso, J. J. 2014, *Monthly Notices of the Royal Astronomical Society*, 445, 4073
- Colless, M., Dalton, G., Maddox, S., et al. 2001, *MNRAS*, 328, 1039
- Costa-Duarte, M. V., Sodr , L., J., & Durret, F. 2011, *MNRAS*, 411, 1716
- Cybulski, R., Yun, M. S., Fazio, G. G., & Gutermuth, R. A. 2014, *MNRAS*, 439, 3564
- Darvish, B., Mobasher, B., Sobral, D., Scoville, N., & Aragon-Calvo, M. 2015, *The Astrophysical Journal*, 805, 121
- Davis, M., Huchra, J., Latham, D. W., & Tonry, J. 1982, *ApJ*, 253, 423
- Dijkstra, E. W. 1959, *Numer. Math.*, 1, 269

³ Data on these systems are available in the electronic version of the paper.

- Doroshkevich, A. G. & Khlopov, M. I. 1984, *MNRAS*, 211, 277
- Dupuy, A., Courtois, H. M., Dupont, F., et al. 2019, *MNRAS*, 489, L1
- Eckert, D., Ettore, S., Pointecouteau, E., et al. 2017, *Astronomische Nachrichten*, 338, 293
- Einasto, J., Suhhonenko, I., Liivamägi, L. J., & Einasto, M. 2019, *A&A*, 623, A97
- Einasto, M., Einasto, J., Tago, E., Müller, V., & Andernach, H. 2001, *AJ*, 122, 2222
- Einasto, M., Lietzen, H., Tempel, E., et al. 2014, *A&A*, 562, A87
- Einasto, M., Saar, E., Martínez, V. J., et al. 2008, *ApJ*, 685, 83
- Eisenstein, D. J., Zehavi, I., Hogg, D. W., et al. 2005, *ApJ*, 633, 560
- Gallazzi, A., Bell, E. F., Wolf, C., et al. 2009, *ApJ*, 690, 1883
- Gavazzi, G., Fumagalli, M., Cucciati, O., & Boselli, A. 2010, *A&A*, 517, A73
- González, R. E. & Padilla, N. D. 2010, *MNRAS*, 407, 1449
- Graham, R. L. & Hell, P. 1985, *Annals of the History of Computing*, 7, 43
- Guenou, L., Adami, C., Durret, F., et al. 2014, *A&A*, 561, A112
- Guglielmo, Poggianti, B. M., Vulcani, B., et al. 2018, *A&A*, 620, A7
- Huchra, J. P., Macri, L. M., Masters, K. L., et al. 2012, *ApJS*, 199, 26
- Huertas-Company, M., Aguerri, J. A. L., Bernardi, M., Mei, S., & Sánchez Almeida, J. 2011, *A&A*, 525, A157
- Kauffmann, G., Heckman, T. M., White, S. D. M., et al. 2003, *MNRAS*, 341, 33
- Klypin, A. A., Trujillo-Gomez, S., & Primack, J. 2011, *ApJ*, 740, 102
- Kopylova, F. G. & Kopylov, A. I. 2006, *Astronomy Letters*, 32, 84
- Kraljic, K., Arnouts, S., Pichon, C., et al. 2018, *MNRAS*, 474, 547
- Kraljic, K., Pichon, C., Dubois, Y., et al. 2019, *MNRAS*, 483, 3227
- Krause, M. O., Ribeiro, A. L. B., & Lopes, P. A. A. 2013, *A&A*, 551, A143
- Kuutma, T., Tamm, A., & Tempel, E. 2017, *A&A*, 600, L6
- Lauer, T. R., Postman, M., Strauss, M. A., Graves, G. J., & Chisari, N. E. 2014, 82
- Libeskind, N. I., van de Weygaert, R., Cautun, M., et al. 2018, *MNRAS*, 473, 1195
- Liivamägi, L. J., Tempel, E., & Saar, E. 2012, *A&A*, 539, A80
- Lintott, C., Schawinski, K., Bamford, S., et al. 2011, *MNRAS*, 410, 166
- Lintott, C. J., Schawinski, K., Slosar, A., et al. 2008, *MNRAS*, 389, 1179
- Luparello, H., Lares, M., Lambas, D. G., & Padilla, N. 2011, *MNRAS*, 415, 964
- Malavasi, N., Arnouts, S., Vibert, D., et al. 2017, *MNRAS*, 465, 3817
- Miller, C. J., Nichol, R. C., Reichart, D., et al. 2005, *The Astronomical Journal*, 130, 968
- Murtagh, F. & Contreras, P. 2011, *Wiley Interdisciplinary Reviews: Data Mining and Knowledge Discovery*, 2, 86
- Murtagh, F. & Legendre, P. 2014, *Journal of Classification*, 31, 274
- Musso, M., Cadiou, C., Pichon, C., et al. 2018, *MNRAS*, 476, 4877
- Peebles, P. J. E. 1980, *The large-scale structure of the universe* (Princeton University Press)
- Planck Collaboration, Ade, P. A. R., Aghanim, N., et al. 2013, *A&A*, 550, A134
- Platen, E., van de Weygaert, R., Jones, B. J. T., Vegter, G., & Calvo, M. A. A. 2011, *MNRAS*, 416, 2494
- Poudel, A., Heinämäki, P., Nurmi, P., et al. 2016, *A&A*, 590, A29
- Rines, K., Diaferio, A., & Natarajan, P. 2007, *ApJ*, 657, 183
- Rines, K., Geller, M. J., Kurtz, M. J., & Diaferio, A. 2003, *AJ*, 126, 2152
- Santanu, R. S. 2014, *Graph Theory with Algorithms and Its Applications: In Applied Science and Technology* (Springer Publishing Company, Incorporated)
- Santiago-Bautista, I., Caretta, C. A., Bravo-Alfaro, H., Pointecouteau, E., & Madrigal, F. 2019, *J. Comp. Int. Sci.*, in press
- Scoville, N., Arnouts, S., Aussel, H., et al. 2013, *The Astrophysical Journal Supplement Series*, 206, 3
- Serna, A. & Gerbal, D. 1996, *A&A*, 309, 65
- Shandarin, S. F. & Zel'dovich, Y. B. 1989, *Rev. Mod. Phys.*, 61, 185
- Smargon, A., Mandelbaum, R., Bahcall, N., & Niederste-Ostholt, M. 2012, *MNRAS*, 423, 856
- Smith, A. G., Hopkins, A. M., Hunstead, R. W., & Pimbblet, K. A. 2012, *MNRAS*, 422, 25
- Sousbie, T. 2011, *MNRAS*, 414, 350
- Springel, V., White, S. D. M., Jenkins, A., et al. 2005, *Nature*, 435, 629
- Strauss, M. A., Weinberg, D. H., Lupton, R. H., et al. 2002, *AJ*, 124, 1810
- Tanaka, M., Hoshi, T., Kodama, T., & Kashikawa, N. 2007, *MNRAS*, 379, 1546
- Tanimura, H., Aghanim, N., Douspis, M., Beelen, A., & Bonjean, V. 2018, 1
- Tempel, E., Stoica, R. S., Martínez, V. J., et al. 2014, *MNRAS*, 438, 3465
- Tempel, E., Tago, E., & Liivamägi, L. J. 2011, 106, 1
- Theodoridis, S. & Koutroumbas, K. 2009, in *Pattern Recognition (Fourth Edition)*, fourth edition edn., ed. T. Sergios & K. Konstantinos (Boston: Academic Press), 595 – 625
- Theodoridis, S., Pikrakis, A., Koutroumbas, K., & Cavouras, D. 2010, *Introduction to Pattern Recognition: A Matlab Approach* (Academic Press)
- Tremonti, C. A., Heckman, T. M., Kauffmann, G., et al. 2004, *ApJ*, 613, 898
- Tully, R. B., Courtois, H., Hoffman, Y., & Pomarède, D. 2014, *Nature*, 513, 71
- Ueda, H. & Itoh, M. 1997, *PASJ*, 49, 131
- Ursino, E., Galeazzi, M., Gupta, A., et al. 2015, *Astrophysical Journal*, 806
- Vogelsberger, M., Genel, S., Springel, V., et al. 2014, *Nature*, 509, 177
- Voronoi, G. 1908, *Journal für die reine und angewandte Mathematik*, 134, 198
- Wang, P., Luo, Y., Kang, X., et al. 2018

Table 8: Main properties of the filaments extracted through GFIF.

Fil. ID (1)	N_{sfil} systems (2)	N_{gfil} gals. (3)	redshift [mean, min, max] (4) (5) (6)			d_{fil} [h_{70}^3 Mpc $^{-3}$] (7)	R_{fil} [h_{70}^{-1} Mpc] (8)	N_{nod} filament skeleton (9) (10)		ℓ_{fil} [h_{70}^{-1} Mpc] (11)
MSCC 55-F1	4	119	0.0619	0.0529	0.0706	0.1570	4.31	3	2	10.5
MSCC 55-F2	3	2	0.0585	0.0527	0.0680	0.1911	0.60	2	2	9.7
MSCC 72-F1	5	257	0.0790	0.0722	0.0868	0.5636	3.57	6	6	28.4
MSCC 72-F2	4	217	0.0801	0.0718	0.0866	0.3688	3.46	5	5	24.6
MSCC 72-F3	5	215	0.0777	0.0717	0.0839	0.3043	3.89	6	5	19.5
MSCC 72-F4	3	140	0.0850	0.0787	0.0917	0.2012	3.49	4	4	26.5
MSCC 175-F1	6	156	0.0912	0.0841	0.0996	0.1541	3.08	8	6	41.8
MSCC 175-F2	3	159	0.0978	0.0885	0.1032	0.2260	3.19	3	3	35.0
MSCC 175-F3	3	87	0.0937	0.0883	0.1001	0.1714	1.79	5	4	47.4
MSCC 175-F4	3	105	0.0923	0.0867	0.0995	0.2184	2.86	3	3	37.5
MSCC 184-F1	5	157	0.1071	0.0994	0.1171	0.0488	2.88	8	5	49.3
MSCC 184-F2	3	61	0.0980	0.0911	0.1029	0.0838	3.09	3	3	39.5
MSCC 211-F1	3	233	0.1205	0.1100	0.1297	0.0465	4.46	13	8	27.9
MSCC 219-F1	10	275	0.1125	0.1063	0.1207	0.1169	2.96	17	6	81.8
MSCC 219-F2	3	4	0.1235	0.1183	0.1287	0.0347	0.79	3	3	40.2
MSCC 222-F1	3	89	0.1422	0.1311	0.1522	0.0418	1.87	14	8	70.0
MSCC 222-F2	5	8	0.1349	0.1238	0.1460	0.0461	0.70	11	8	78.8
MSCC 223-F1	3	11	0.1367	0.1286	0.1472	0.0245	0.86	12	8	48.7
MSCC 229-F1	3	32	0.1445	0.1361	0.1514	0.0389	1.96	9	6	63.1
MSCC 236-F1	5	231	0.0324	0.0228	0.0415	0.3382	1.49	16	9	39.3
MSCC 236-F2	4	324	0.0411	0.0361	0.0461	0.2409	2.65	7	6	38.5
MSCC 236-F3	5	286	0.0331	0.0274	0.0399	0.4889	2.62	8	5	20.0
MSCC 236-F4	3	150	0.0296	0.0255	0.0364	0.3971	2.24	5	4	19.6
MSCC 236-F5	3	188	0.0354	0.0286	0.0422	0.4448	2.47	5	5	20.8
MSCC 236-F6	3	318	0.0330	0.0276	0.0373	2.3032	2.66	2	2	16.8
MSCC 236-F7	3	103	0.0333	0.0297	0.0391	0.4359	1.53	4	3	16.4
MSCC 238-F1	5	174	0.1190	0.1075	0.1309	0.0558	2.95	11	7	85.3
MSCC 238-F2	6	201	0.0915	0.0802	0.1010	0.0928	2.98	14	10	76.1
MSCC 238-F3	3	155	0.1054	0.0979	0.1115	0.0782	2.64	11	8	99.0
MSCC 238-F4	3	3	0.0957	0.0896	0.1024	0.1467	0.71	3	3	28.6
MSCC 238-F5	3	4	0.1016	0.0934	0.1099	0.0285	0.67	3	2	32.5
MSCC 238-F6	3	7	0.1096	0.1040	0.1156	0.0398	0.88	4	3	30.4
MSCC 248-F1	3	159	0.1256	0.1161	0.1355	0.0895	3.35	10	7	82.1
MSCC 266-F1	5	132	0.1282	0.1188	0.1344	0.0366	2.94	9	8	75.8
MSCC 272-F1	6	374	0.0752	0.0694	0.0808	0.8405	2.93	6	4	17.5
MSCC 272-F2	3	79	0.0757	0.0714	0.0814	0.1245	2.66	4	3	10.3
MSCC 277-F1	10	384	0.1124	0.1031	0.1208	0.1268	2.99	21	11	89.3
MSCC 277-F2	5	227	0.1053	0.0956	0.1135	0.0805	2.93	16	10	69.0
MSCC 278-F1	7	956	0.0328	0.0251	0.0398	0.9871	2.41	36	14	56.3
MSCC 278-F2	3	292	0.0322	0.0273	0.0361	0.4963	1.70	24	13	20.8
MSCC 278-F3	4	145	0.0319	0.0266	0.0386	0.3810	1.18	14	7	24.4
MSCC 278-F4	8	629	0.0254	0.0221	0.0298	1.0335	1.86	27	10	36.9
MSCC 278-F5	3	122	0.0348	0.0297	0.0387	0.4401	1.76	7	6	11.1
MSCC 283-F1	4	165	0.1339	0.1245	0.1470	0.0701	3.96	7	4	47.7
MSCC 283-F2	5	94	0.1364	0.1284	0.1465	0.0655	3.26	6	5	49.1
MSCC 283-F3	3	4	0.1357	0.1296	0.1496	0.0397	0.96	2	2	24.2
MSCC 295-F1	7	1020	0.0230	0.0160	0.0284	2.1243	1.89	37	28	44.6
MSCC 295-F2	7	1289	0.0228	0.0158	0.0299	2.2694	2.37	34	12	18.2
MSCC 295-F3	4	497	0.0232	0.0189	0.0283	0.5824	1.36	44	17	26.5
MSCC 295-F4	4	186	0.0218	0.0188	0.0255	0.6254	1.83	10	9	30.8
MSCC 310-F1	10	499	0.0609	0.0518	0.0689	0.4180	2.81	18	11	61.6
MSCC 310-F2	8	523	0.0502	0.0443	0.0588	0.5210	2.84	22	11	51.8
MSCC 310-F3	7	407	0.0481	0.0427	0.0528	0.3486	2.50	19	10	49.0
MSCC 310-F4	8	313	0.0656	0.0585	0.0710	0.4263	2.46	14	10	59.0
MSCC 310-F5	7	325	0.0700	0.0642	0.0774	0.5303	2.60	13	7	47.6
MSCC 310-F6	6	243	0.0725	0.0651	0.0791	0.2986	1.97	12	9	39.3
MSCC 310-F7	4	219	0.0551	0.0479	0.0619	0.4062	2.76	7	5	20.7
MSCC 310-F8	4	164	0.0546	0.0485	0.0617	0.2118	2.22	9	7	33.7
MSCC 310-F9	4	124	0.0464	0.0437	0.0528	0.1464	1.13	9	6	17.9
MSCC 311-F1	13	607	0.0813	0.0753	0.0892	0.2812	3.54	14	9	74.5
MSCC 311-F2	5	254	0.0847	0.0769	0.0937	0.3235	3.69	4	3	23.5
MSCC 311-F3	3	138	0.0888	0.0821	0.0937	0.1900	4.32	2	2	15.3
MSCC 311-F4	3	119	0.0826	0.0746	0.0901	0.2447	3.58	2	2	19.5
MSCC 314-F1	4	46	0.0819	0.0769	0.0893	0.1201	1.88	4	4	29.6

Continued on next page

Table 8 – continued from previous page

Fil. ID	N_{sfil} systems	N_{gfil} gals.	redshift [mean, min, max]	d_{fil} [h_{70}^3 Mpc $^{-3}$]	R_{fil} [h_{70}^{-1} Mpc]	N_{nod} filament	N_{nod} skeleton	ℓ_{fil} [h_{70}^{-1} Mpc]		
(1)	(2)	(3)	(4)	(5)	(6)	(7)	(8)	(9)	(10)	(11)
MSCC 314-F2	3	66	0.0777	0.0715	0.0844	0.1610	2.78	2	2	12.3
MSCC 317-F1	4	55	0.1331	0.1224	0.1417	0.0282	1.73	15	10	71.7
MSCC 317-F2	4	8	0.1187	0.1102	0.1264	0.0528	0.69	10	7	75.5
MSCC 323-F1	7	223	0.1380	0.1262	0.1540	0.0436	3.73	14	11	129.3
MSCC 323-F2	3	16	0.1383	0.1309	0.1535	0.0261	1.66	5	4	29.4
MSCC 333-F1	3	82	0.0760	0.0723	0.0833	0.1205	2.36	5	4	29.8
MSCC 333-F2	4	117	0.0803	0.0752	0.0880	0.1519	2.83	5	4	24.5
MSCC 333-F3	4	83	0.0794	0.0729	0.0835	0.2052	2.46	5	5	34.6
MSCC 335-F1	10	345	0.0779	0.0705	0.0843	0.1260	2.60	21	11	105.0
MSCC 335-F2	4	22	0.0665	0.0613	0.0731	0.0650	0.75	9	8	83.8
MSCC 335-F3	4	111	0.0762	0.0712	0.0814	0.1113	2.45	6	4	45.9
MSCC 343-F1	4	115	0.0822	0.0786	0.0874	0.1394	2.51	7	6	28.7
MSCC 343-F2	3	95	0.0798	0.0733	0.0876	0.2638	2.50	3	3	19.3
MSCC 343-F3	3	125	0.0824	0.0738	0.0876	0.1991	2.65	6	5	15.6
MSCC 360-F1	4	182	0.1050	0.0967	0.1159	0.1367	2.95	9	6	60.8
MSCC 360-F2	3	31	0.1074	0.1004	0.1152	0.0870	1.52	6	4	49.3
MSCC 360-F3	3	5	0.1033	0.0973	0.1093	0.0416	1.46	3	2	29.9
MSCC 386-F1	7	346	0.0734	0.0657	0.0805	0.4163	2.91	18	10	34.0
MSCC 386-F2	4	115	0.0708	0.0636	0.0765	0.1969	1.92	10	8	39.6
MSCC 386-F3	5	129	0.0627	0.0591	0.0705	0.1760	1.56	13	10	43.2
MSCC 386-F4	4	46	0.0617	0.0594	0.0664	0.1703	0.92	7	6	21.3
MSCC 407-F1	5	101	0.1388	0.1254	0.1468	0.0177	3.61	10	6	59.2
MSCC 414-F1	4	420	0.0626	0.0537	0.0691	0.6269	2.51	19	9	38.1
MSCC 414-F2	6	243	0.0628	0.0548	0.0667	0.3793	2.54	12	7	34.0
MSCC 414-F3	6	240	0.0750	0.0688	0.0809	0.5198	2.53	12	7	27.1
MSCC 414-F4	5	196	0.0641	0.0585	0.0675	0.3705	2.52	10	5	13.5
MSCC 414-F5	4	243	0.0748	0.0684	0.0810	0.4251	2.53	10	8	22.1
MSCC 414-F6	3	126	0.0657	0.0613	0.0701	0.3368	2.01	7	6	22.9
MSCC 414-F7	3	118	0.0616	0.0576	0.0647	0.2329	1.97	10	5	14.1
MSCC 414-F8	3	72	0.0657	0.0603	0.0722	0.1197	1.82	7	6	29.9
MSCC 414-F9	4	116	0.0663	0.0594	0.0726	0.3001	2.50	5	5	22.9
MSCC 414-F10	4	107	0.0546	0.0518	0.0590	0.4163	1.99	6	6	29.9
MSCC 414-F11	5	147	0.0616	0.0589	0.0657	0.1262	1.64	14	8	35.1
MSCC 414-F12	3	14	0.0762	0.0696	0.0801	0.1126	0.66	4	4	9.8
MSCC 414-F13	4	66	0.0640	0.0614	0.0674	0.1692	1.94	4	4	19.2
MSCC 414-F14	4	93	0.0727	0.0686	0.0758	0.4275	1.78	7	6	23.6
MSCC 414-F15	3	31	0.0607	0.0563	0.0640	0.1070	1.80	3	3	9.0
MSCC 419-F1	3	130	0.1139	0.1084	0.1210	0.1849	4.03	2	2	12.8
MSCC 419-F2	3	88	0.1099	0.1044	0.1182	0.1816	3.20	2	2	18.1
MSCC 419-F3	4	36	0.1127	0.1080	0.1191	0.0693	1.79	5	4	25.2
MSCC 422-F1	3	11	0.1424	0.1321	0.1528	0.0291	0.95	8	6	45.0
MSCC 430-F1	4	151	0.0975	0.0880	0.1066	0.1391	2.78	7	4	39.2
MSCC 430-F2	4	23	0.0937	0.0867	0.0999	0.1684	1.50	5	4	41.1
MSCC 430-F3	3	12	0.0942	0.0891	0.1015	0.0691	1.89	2	2	21.2
MSCC 430-F4	3	0	0.1024	0.0973	0.1041	0.0225	0.00	2	2	18.3
MSCC 440-F1	6	184	0.1173	0.1074	0.1284	0.1550	2.93	8	6	50.2
MSCC 454-F1	13	687	0.0389	0.0334	0.0466	2.7338	2.39	23	13	63.5
MSCC 454-F2	6	498	0.0446	0.0377	0.0500	2.3032	2.57	20	9	29.1
MSCC 454-F3	3	146	0.0520	0.0464	0.0557	4.0214	2.48	3	3	9.3
MSCC 454-F4	3	146	0.0490	0.0425	0.0551	1.5093	2.42	3	3	12.8
MSCC 454-F5	3	39	0.0438	0.0424	0.0460	1.1194	0.83	3	3	8.6
MSCC 457-F1	19	908	0.0786	0.0709	0.0877	0.4021	3.37	23	11	78.4
MSCC 457-F2	8	256	0.0758	0.0673	0.0830	0.1594	2.69	12	8	52.5
MSCC 457-F3	6	179	0.0846	0.0768	0.0896	0.2454	2.48	7	5	30.6
MSCC 457-F4	3	92	0.0829	0.0757	0.0881	0.1691	2.80	3	3	22.2
MSCC 457-F5	3	77	0.0756	0.0676	0.0785	0.0982	1.97	3	3	16.8
MSCC 457-F6	3	13	0.0816	0.0779	0.0872	0.0649	0.74	3	3	23.3
MSCC 460-F1	12	536	0.1142	0.1067	0.1242	0.1862	3.61	17	9	69.3
MSCC 460-F2	6	214	0.1139	0.1043	0.1237	0.1195	3.62	9	6	57.9
MSCC 460-F3	6	82	0.1080	0.1003	0.1159	0.0695	2.55	6	5	59.7
MSCC 460-F4	5	63	0.1218	0.1155	0.1304	0.0522	2.51	7	5	27.6
MSCC 463-F1	9	489	0.0722	0.0652	0.0788	0.3732	2.77	16	10	57.4
MSCC 463-F2	6	352	0.0765	0.0699	0.0839	0.3129	2.67	15	10	39.0
MSCC 463-F3	11	313	0.0768	0.0696	0.0842	0.2787	2.27	13	11	73.6
MSCC 463-F4	3	234	0.0657	0.0585	0.0743	0.4589	2.77	5	4	20.8

Continued on next page

Table 8 – continued from previous page

Fil. ID (1)	N_{sfil} systems (2)	N_{gfil} gals. (3)	redshift [mean, min, max] (4) (5) (6)			d_{fil} [$h_{70}^3 \text{ Mpc}^{-3}$] (7)	R_{fil} [$h_{70}^{-1} \text{ Mpc}$] (8)	N_{nod} filament skeleton (9) (10)		ℓ_{fil} [$h_{70}^{-1} \text{ Mpc}$] (11)
MSCC 463-F5	5	192	0.0655	0.0600	0.0730	0.4039	2.08	10	8	41.9
MSCC 463-F6	7	233	0.0837	0.0775	0.0894	0.2868	2.56	7	6	36.9
MSCC 463-F7	4	8	0.0688	0.0654	0.0739	0.0878	0.68	8	7	26.8
MSCC 463-F8	4	119	0.0663	0.0628	0.0698	0.4765	2.59	6	4	12.5
MSCC 463-F9	4	99	0.0706	0.0660	0.0764	0.2416	1.87	6	5	31.9
MSCC 463-F10	3	83	0.0701	0.0651	0.0754	0.3595	2.05	4	3	12.7
MSCC 463-F11	3	106	0.0802	0.0748	0.0861	0.1864	2.64	4	4	14.8
MSCC 474-F1	3	881	0.0369	0.0300	0.0444	2.7548	2.63	13	5	10.5
MSCC 474-F2	5	407	0.0340	0.0296	0.0387	1.3043	2.06	13	7	23.4
MSCC 474-F3	3	147	0.0368	0.0318	0.0412	0.2423	1.98	9	8	16.5
MSCC 474-F4	3	176	0.0321	0.0284	0.0388	0.7372	1.75	7	5	16.5
MSCC 474-F5	3	114	0.0337	0.0292	0.0372	0.3332	1.51	10	6	17.2
MSCC 474-F6	4	193	0.0365	0.0324	0.0423	0.5697	1.90	6	6	15.3
MSCC 474-F7	3	0	0.0379	0.0328	0.0406	0.1777	0.00	10	7	28.3
MSCC 484-F1	4	109	0.1361	0.1243	0.1501	0.0130	3.89	7	6	54.6

Notes.

- (1) ID of the filament;
- (2) number of systems detected by GSyF linked by the filament;
- (3) number of galaxies attributed to the filament;
- (4) to (6) mean, min. and max. redshift of the filament;
- (7) mean galaxy number density inside the filament;
- (8) mean transversal radius of the filament measured at $10 \times d$;
- (9) and (10) number of nodes that constitute the filament and its central skeleton;
- (11) length of the filament skeleton.